A General Circulation Model for Upper Ocean Simulation

A. ROSATI AND K. MIYAKODA

Geophysical Fluid Dynamics Laboratory/NOAA, Princeton University, Princeton, New Jersey

(Manuscript received 20 October 1987, in final form 3 May 1988)

ABSTRACT

A general circulation model (GCM) of the ocean that emphasizes the simulation of the upper ocean has been developed. This emphasis is in keeping with its future intent, that of an air–sea coupled model. The basic model is the primitive equation model of Bryan and Cox with the additions, of optional usage, of the Mellor–Yamada level 2.5 turbulence closure scheme and horizontal nonlinear viscosity. These modifications are intended to improve the upper ocean simulations, particularly sea surface temperature and heat content. The horizontal grid spacing is 1° latitude × 1° longitude and is global in domain. The equatorial region between 10°N and 10°S is further refined in the north–south direction to ½° resolution. There are 12 vertical levels, with six levels in the top 70 m. The model incorporates varying bottom topography.

Prior to coupling the ocean model to an atmospheric GCM, experiments have been carried out to determine the ocean GCM's performance using atmospheric forcing from observed data. The data source was the National Meteorological Center twice daily 1000 mb analysis for winds, temperature, and relative humidity for 1982 and 1983. From these data, wind stress and total heat flux were calculated from bulk formulas and used as surface boundary conditions for the ocean model.

The response of the ocean GCM to mixing parameterization schemes and frequency of atmospheric forcing have been examined. In particular, the use of constant eddy coefficients for both horizontal and vertical mixing (A-model) versus nonlinear horizontal viscosity and turbulence closure schemes (E-model) have been examined, along with comparisons of monthly mean versus 12-hourly forcing. It was found that, in general, the E-physics produces a more realistic mixed-layer structure as compared to A-physics. Using the monthly mean values produces sea surface temperatures that are too warm, presumably because the evaporative flux, which is proportional to the wind speed, is underestimated. The 12-h forcing improves appreciably both the A and E model since the heat flux is better represented; the E-case shows an even greater improvement due to its sensitivity to wind stirring. The near surface heat budget, along with more traditional variables, is examined for a short period during the 1982–83 El Niño event. These results are encouraging considering the many possible sources of error, including those in forcing data, initial conditions, radiative fluxes, and bulk exchange coefficients.

1. Introduction

For weather forecasting on time scales of a few days, the primary variability is due to the initial state of the atmosphere. As the time scale increases to a month and beyond, the memory of the atmospheric initial state is gradually lost, and the general nature of the long period fluctuations is to a large extent determined by the slowly varying boundary at the air–sea interface. In large-scale air–sea interactions, the ocean primarily supplies moisture and heat to the atmosphere, whereas the atmosphere supplies momentum, heat, and fresh water to the ocean. This implies that within this closed feedback system, for the heat exchange to the atmosphere to be reasonably accurate, the upper-ocean thermodynamics must be well represented. A recent study by White et al. (1987) suggests that the redistribution of upper-ocean heat content in the western tropical Pacific may be an important factor in the evolution of ENSO events, showing the necessity for models to simulate the upper ocean well so that the changes in heat content may be properly represented.

One-dimensional models of the upper ocean, which include turbulent mixing processes and local atmospheric forcing, are quite capable of producing realistic simulations of SST (sea surface temperature) over a large portion of the world's oceans (Garwood 1979; Miyakoda and Rosati 1984). However, these models do not have the same success in regions where the redistribution of heat, due to the dynamics, plays a crucial role in influencing SST (Meehl and Washington 1985). Thus, we combine an ocean GCM that simulates the large-scale ocean circulation with a mixed-layer model that focuses on the vertical mixing process to simulate the locally forced response in the ocean boundary layer. This combination yields a model that includes both dynamical and thermodynamical processes. There have been attempts by other investigators at incorporating primitive equation dynamics and a parameterization of mixed-layer physics in regional models. Adamec et al. (1981) and Schopf and Cane (1983) used bulk

Corresponding author address: Dr. Anthony Rosati, Geophysical Fluid Dynamics Laboratory/NOAA, Princeton University, P.O. Box 308, Princeton, NJ 08542.

mixed-layer physics to simulate the response of the ocean to a hurricane and to study the interplay between the dynamics and mixed-layer physics in the equatorial ocean, respectively. Pacanowski and Philander (1981), in a multi-layer model, used a Richardson-number-dependent eddy viscosity parameterization in equatorial studies. Sarmiento (1986) included this parameterization for the Atlantic Ocean. Haney (1985) also used a Richardson-number-based parameterization combined with a multilevel primitive-equation ocean circulation model to study the interannual variability of SST in the central North Pacific Ocean. Blumberg and Mellor (1983) incorporated the Mellor–Yamada level 2.5 turbulence closure scheme to their coastal ocean models. Their approach is very similar to the one we have taken, but for a limited domain.

The long range goal, which has driven the development of this GCM, is the creation of an air–sea model that is suitable for seasonal forecasts. For the seasonal time scale, the tropical Pacific Ocean would be of prime importance; therefore, a limited domain model covering this region could be embedded in a climatological ocean. Instead, choosing a global domain frees up the need for artificial boundary constraints, allows for effects from both midlatitude and tropics over all oceans, and removes the guesswork as to where the interactive effects are important.

In this paper, a description of the model and the external forcings is given in sections 2 and 3. As a first step toward the development of a coupled air–sea model, it is desirable to study the effects the subgrid-scale physics and atmospheric forcing have on the model. Experiments investigating these effects were run and are examined in section 4. Section 5 considers the near-surface heat balance. Some of the results of the 1982–83 run are reported in section 6.

2. Description of the model

a. Design considerations

Since the atmospheric model only feels the ocean through the SST, it is important that the ocean GCM have an accurate upper ocean simulation. Such a strategy dictates that the model be of high resolution both horizontally and vertically in order to resolve the equatorial flow properly and to represent mixed-layer processes adequately. Also, considering that the ocean in the mixed layer is closely tied to the atmosphere, the observed atmospheric boundary forcing, both wind stress and heat flux, needs to be treated carefully. These guidelines have governed the design of the ocean GCM described herein.

One of the important and difficult modeling issues concerns the sensitivity of an ocean GCM to parameterizations of subgrid-scale processes. Here we contrast the use of constant eddy coefficients (A-physics) with nonlinear horizontal viscosity together with the vertical mixing determined from a turbulence closure scheme (E-physics). Miyakoda and Sirutis (1977, 1983) used this notation, for an atmospheric model, in their study describing a similar hierarchy of mixing parameterizations.

b. Governing equations

The model is a modified version of the numerical model described in Bryan (1969) and made efficient for modern computers by Cox (1984). Only the equations governing the ocean circulation will be given here, but a more detailed description may be found in the previously mentioned references. Two simplifying approximations to the Navier–Stokes (primitive equations) equations are, first, it is assumed that the weight of the fluid identically balances the pressure (hydrostatic assumption), and second, density differences are neglected unless they are multiplied by gravity (Boussinesq approximation). A spherical coordinate system is used, with λ, ϕ and z representing longitude, latitude, and height. Let $m = \sec\phi$, $n = \sin\phi$ and a be the radius of the Earth. Then the equations for velocity (u, v), temperature T, and salinity s are

$$\frac{\partial u}{\partial t} + \mathcal{L}(u) - \left(\frac{u\tan\phi}{a} + 2\Omega n\right)v = -ma^{-1}\rho_0^{-1}\frac{\partial p}{\partial \lambda} + \frac{\partial}{\partial z}\left(-\overline{wu} + \nu\frac{\partial u}{\partial z}\right) + F\lambda, \quad (2.1)$$

$$\frac{\partial v}{\partial t} + \mathcal{L}(v) + \left(\frac{u\tan\phi}{a} + 2\Omega n\right)u = -a^{-1}\rho_0^{-1}\frac{\partial p}{\partial \phi} + \frac{\partial}{\partial z}\left(-\overline{wv} + \nu\frac{\partial v}{\partial z}\right) + F\phi, \quad (2.2)$$

$$\frac{\partial T}{\partial t} + \mathcal{L}(T) = \frac{\partial}{\partial z}\left(-\overline{wT} + \nu_T\frac{\partial T}{\partial z}\right) + \frac{1}{\rho_0 c_p}\frac{\partial I}{\partial z} + F_T, \quad (2.3)$$

$$\frac{\partial s}{\partial t} + \mathcal{L}(s) = \frac{\partial}{\partial z}\left(-\overline{ws} + \nu_s\frac{\partial s}{\partial z}\right) + F_s, \quad (2.4)$$

where the advection operator, $\mathcal{L}$, is represented by

$$\mathcal{L}(\mu) = ma^{-1}\left[\frac{\partial}{\partial\lambda}(u\mu) + \frac{\partial}{\partial\phi}(v\mu m^{-1})\right] + \frac{\partial}{\partial z}(w\mu), \quad (2.5)$$

where μ is an arbitrary variable. The continuity equation is

$$\mathcal{L}(1) = 0. \quad (2.6)$$

The hydrostatic equation and the equation of state are

$$\frac{\partial p}{\partial z} = -\rho g, \quad (2.7)$$

$$p = p(T, s, \rho). \quad (2.8)$$

Here t is time, p is pressure, ρ is density, ν is kinematic viscosity, ν_T and ν_s are the thermal and salt diffusivities, c_p is specific heat, ρ_0 is a reference value of density, and I is the downward solar irradiance. Following Mellor and Yamada (1974, 1982), the level 2.5 closure turbulence is characterized by

$$\frac{\partial b^2}{\partial t} + \mathcal{L}(b^2) = \frac{\partial}{\partial z}\left(K_b \frac{\partial b^2}{\partial z}\right) - 2\overline{wu}\frac{\partial u}{\partial z} - 2\overline{wv}\frac{\partial v}{\partial z} - 2\frac{g}{\rho_0}\overline{w\rho} - \frac{2b^3}{B_1 l} + F_b, \quad (2.9)$$

$$\frac{\partial b^2 l}{\partial t} + \mathcal{L}(b^2 l) = \frac{\partial}{\partial z}\left(K_b \frac{\partial b^2 l}{\partial z}\right) + lE_1\left[-\overline{wu}\frac{\partial u}{\partial z} - \overline{wv}\frac{\partial v}{\partial z} - E_3\left(\frac{g}{\rho_0}\overline{w\rho}\right)\right] - \tilde{w}\frac{b^3}{B_1} + F_l, \quad (2.10)$$

where b^2 is twice the turbulence kinetic energy (TKE), l is the turbulence length scale, and E_1, E_3 and B_1 are empirical constants. For the quantity b^2 or $b^2 l$, the terms above represent the local rate of change (terms 1 and 2), the diffusion of the quantity (term 3), production of the quantity due to mean shear (terms 4 and 5), production of the quantity due to buoyancy (term 6), and dissipation of the quantity (term 7). The fluxes are given by

$$(-\overline{wu}, -\overline{wv}) = K_M\left(\frac{\partial u}{\partial z}, \frac{\partial v}{\partial z}\right), \quad (2.11a,b)$$

$$-\overline{w\rho} = K_H \frac{\partial \rho}{\partial z}. \quad (2.12)$$

The correlation equations for temperature and salinity are assumed identical to those for density; therefore,

$$-\overline{wT} = K_H \frac{\partial T}{\partial z}, \quad (2.13)$$

$$-\overline{ws} = K_H \frac{\partial s}{\partial z}, \quad (2.14)$$

where

$$K_M \equiv lbs_M \quad \text{and} \quad K_H \equiv lbs_H. \quad (2.15a,b)$$

The stability factors s_M and s_H are analytically derived, algebraic relations derived from closure hypotheses described in Mellor and Yamada (1982). The remaining unknown is K_b in (2.9) and (2.10) and is defined analogous to (2.15a, b) so that

$$K_b \equiv lbs_b, \quad (2.16)$$

where $s_b = 0.2 s_M/0.392$ (note that for the neutral case where turbulent production is balanced by dissipation, $s_M = 0.392$ and $s_b = 0.2$). In (2.10), $\tilde{w}$ is a "wall proximity" function defined as

$$\tilde{w} = 1 + E_2(l/L)^2, \quad (2.17)$$

where E_2 is an empirical constant, $L = k_0 z$, and k_0 is the von Karman constant. Near a surface, $l \sim k_0 z$ so that $\tilde{w} = 1 + E_2$, whereas far from the surface $l \ll L$, $\tilde{w} \sim 1$.

In the case of the A-physics, it is not necessary to solve (2.9) and (2.10), and the vertical mixing coefficients are taken to be constant with $K_M = 30\ \text{cm}^2\ \text{s}^{-1}$ and $K_H = 1\ \text{cm}^2\ \text{s}^{-1}$.

The terms F_λ, F_ϕ, F_T, F_s, F_b and F_l, found in (2.1), (2.2), (2.3), (2.4), (2.9) and (2.10), represent horizontal subgrid-scale mixing and are all treated linearly in the A-physics; however, for the E-physics, F_λ, F_ϕ, F_T and F_s are treated by using an adaptation of the scheme proposed by Smagorinsky (1963). According to Smagorinsky (1963) and Deardorff (1973), the ratio of change of the east–west and north–south momentum, resulting from the horizontal stresses appearing in (2.1) and (2.2), are computed as

$$F_\lambda = ma^{-1}\left[\frac{\partial(\tau^{\lambda\lambda})}{\partial\lambda} + m\frac{\partial(\tau^{\lambda\phi}\cos^2\phi)}{\partial\phi}\right], \quad (2.18)$$

$$F_\phi = ma^{-1}\left[\frac{\partial(\tau^{\phi\lambda})}{\partial\lambda} + \frac{\partial(\tau^{\phi\phi}\cos\phi)}{\partial\phi} + \sin\phi\tau^{\lambda\lambda}\right], \quad (2.19)$$

where $\tau^{\lambda\lambda}$, $\tau^{\lambda\phi}$, $\tau^{\phi\lambda}$ and $\tau^{\phi\phi}$ denote the stress tensors. We can express them by

$$\tau^{\lambda\lambda} = A_M{}^{\lambda} D_T, \quad (2.20)$$

$$\tau^{\lambda\phi} = A_M{}^{\phi} D_s, \quad (2.21)$$

$$\tau^{\phi\lambda} = A_M{}^{\lambda} D_s, \quad (2.22)$$

$$\tau^{\phi\phi} = -A_M{}^{\phi} D_T, \quad (2.23)$$

where the tension and shearing rates of strain, respectively, are defined as

$$D_T = ma^{-1}\frac{\partial u}{\partial\lambda} - m^{-1}a^{-1}\frac{\partial(mv)}{\partial\phi}, \quad (2.24)$$

$$D_s = ma^{-1}\frac{\partial v}{\partial\lambda} + m^{-1}a^{-1}\frac{\partial(mu)}{\partial\phi}. \quad (2.25)$$

In this formulation, the horizontal eddy-diffusion coefficient is proportional to the horizontal grid length and to the local deformation rate. Thus, in (2.20)–(2.23), $A_M{}^{\lambda}$ and $A_M{}^{\phi}$ are defined by

$$A_M{}^{\lambda} = c^{\lambda}|D|, \quad (2.26)$$

$$A_M{}^{\phi} = c^{\phi}|D|, \quad (2.27)$$

where c^{λ} and c^{ϕ} are proportional to the square of the respective grid increments $\Delta\lambda$ and $\Delta\phi$ and to an empirical constant c, the $|D|$ is total deformation, i.e., $D^2 = 2(D_s^2 + D_T^2)$. The factors c^{λ} and c^{ϕ} are given by

$$c^{\lambda} = (cma\Delta\lambda)^2/2, \quad (2.28)$$

$$c^{\phi} = (ca\Delta\phi)^2/2. \quad (2.29)$$

The value for c was chosen to be 0.14.

In the A-physics version, the horizontal subgrid-scale mixing is treated using linear viscosity. In this case, the horizontal stresses are written as

$$\tau^{\lambda\lambda} = A_M\left(ma^{-1}\frac{\partial u}{\partial\lambda} - \frac{\tan\phi}{a}v\right), \quad (2.30)$$

$$\tau^{\lambda\phi} = A_M m^{-1}a^{-1}\frac{\partial(mu)}{\partial\phi}, \quad (2.31)$$

$$\tau^{\phi\lambda} = A_M ma^{-1}\frac{\partial v}{\partial\lambda}, \quad (2.32)$$

$$\tau^{\phi\phi} = A_M ma^{-1}\frac{\partial v}{\partial\phi}, \quad (2.33)$$

where A_M is constant and is equal to 10^8 cm^2 s^{-1}.

The equation for the formulation of horizontal subgrid-scale diffusion is

$$F_\alpha = ma^{-1}\frac{\partial}{\partial\lambda}\left(A_\alpha{}^\lambda ma^{-1}\frac{\partial\alpha}{\partial\lambda}\right) + ma^{-1}\frac{\partial}{\partial\phi}\left(A_\alpha{}^\phi ma^{-1}\frac{\partial\alpha}{\partial\phi}\right), \quad (2.34)$$

where α stands for either temperature, salinity, turbulent kinetic energy, or turbulent macroscale,

$$A_\alpha{}^\lambda = \gamma_1 A_M{}^\lambda, \quad (2.35)$$

$$A_\alpha{}^\phi = \gamma_1 A_M{}^\phi, \quad (2.36)$$

where γ_1 is simply taken to be unity for this case. For the E-physics, $A_M{}^\lambda$ and $A_M{}^\phi$ are taken from (2.26) and (2.27). In the linear (A-physics) case, both $A_\alpha{}^\lambda$ and $A_\alpha{}^\phi$ are taken as constant and equal to 10^7 cm^2 s^{-1}. Both F_b and F_l always use the linear form with $A_\alpha{}^\lambda = A_\alpha{}^\phi = 10^8$ cm^2 s^{-1}.

c. *Boundary conditions*

The boundary conditions at the ocean surface ($z = 0$) are

$$\rho_0 K_M\left(\frac{\partial u}{\partial z}, \frac{\partial v}{\partial z}\right) = (\tau^\lambda, \tau^\phi), \quad (2.37)$$

$$\rho_0 c_p K_H\frac{\partial T}{\partial z} = Q_u, \quad (2.38)$$

$$\rho_0 c_p K_H\frac{\partial s}{\partial z} = \mu(s^* - s), \quad (2.39)$$

$$b^2 = B_1{}^{2/3}u_*^2, \quad (2.40)$$

$$b^2 l = 0, \quad (2.41)$$

$$w = 0, \quad (2.42)$$

$$I = Q_s, \quad (2.43)$$

where $(\tau^\lambda, \tau^\phi)$ are the zonal and meridional components of wind stress, Q_u is the net upward surface heat flux (see section 3), s^* is the climatological salinity taken from the atlas of Levitus (1982), and μ is an inverse time scale. In (2.40), $u_* = |\tau/\rho_0|^{1/2}$ is the friction velocity and B_1 is one of the empirical constants in the turbulence closure relations. The "rigid lid" assumption (2.42) filters out high-speed external gravity waves, thus allowing for a larger time step. The value Q_s is the solar irradiance at the surface. Poleward of 55°, the surface heat flux is computed the same way as the salt flux (2.39), but we use climatological SST from Levitus (1982). Temperatures are not allowed to be less than −2.0°C. This is to account for sea ice, which the model presently does not compute.

At the ocean bottom, $z = -H$, fluxes of heat and salt are taken to be zero:

$$K_H\left(\frac{\partial T}{\partial z}, \frac{\partial s}{\partial z}\right) = 0; \quad (2.44)$$

also,

$$b^2 = 0, \quad (2.45)$$

$$b^2 l = 0. \quad (2.46)$$

The horizontal velocities are not set to zero at the bottom; instead, a bottom stress condition is applied:

$$\rho_0 K_M\frac{\partial}{\partial z}(u, v) = (\tau_B{}^\lambda, \tau_B{}^\phi) = k(u, v)|\mathbf{V}| \quad \text{at} \quad z = -H, \quad (2.47)$$

where $(\tau_B{}^\lambda, \tau_B{}^\phi)$ are bottom stress components and $k = 0.0013$. Also at the bottom,

$$w = -mua^{-1}\frac{\partial H}{\partial\lambda} - va^{-1}\frac{\partial H}{\partial\phi}, \quad (2.48)$$

which results from requiring the flow to be parallel to the slope.

At lateral walls, a no-slip condition is imposed and no flux of heat or salt is allowed, so

$$u = v = \frac{\partial T}{\partial n} = \frac{\partial s}{\partial n} = 0 \quad (2.49)$$

where $\partial(\ )/\partial n$ represents the local derivative normal to the wall.

d. *Numerical methodology and grids*

The governing equations, along with their boundary conditions, are solved by finite difference techniques with a staggered "B" grid configuration (Arakawa and Lamb 1977; Mesinger and Arakawa 1976; Wajsowicz 1986). The time differencing is centered, i.e., leapfrog. However, the scheme is quasi-implicit in that the vertical diffusion is evaluated at the forward time level. Thus, small vertical spacing is permissible near the surface without the need to reduce the time increment or restrict the magnitude of the mixing coefficients.

The finite difference scheme is energetically consistent and is second-order accurate in space and time. Details of the finite difference equations may be found in Bryan (1969), Semtner (1974), and Cox (1984).

The world ocean is discretized onto a computational grid with a horizontal resolution of 1° longitude × 1° latitude but with ⅓° latitudinal resolution within the 10°N–10°S equatorial band. The vertical layers vary in thickness to accommodate more resolution near the surface. There are 12 levels so that the layers thicken from 5 m at the surface to 1140 m at 3000 m depth, with eight of the levels in the top 248 m. Since the model has 12 vertical levels, the actual topographic data was fitted to the nearest model level. All depths less than 25 m were considered to be land areas. The maximum ocean depth is taken as 3000 m. The distribution of the grid points in the vertical is illustrated in Fig. 1, with dashed lines indicating the depth at which the turbulence quantities and vertical velocity are defined and the solid lines corresponding to the depth at which horizontal velocity, temperature, and salinity are located. One clear deficiency with this resolution is the small number of grid points between 69 and 248 m, which does not allow for the equatorial undercurrent to be resolved properly. In the near future the vertical resolution will be increased to alleviate this inadequacy.

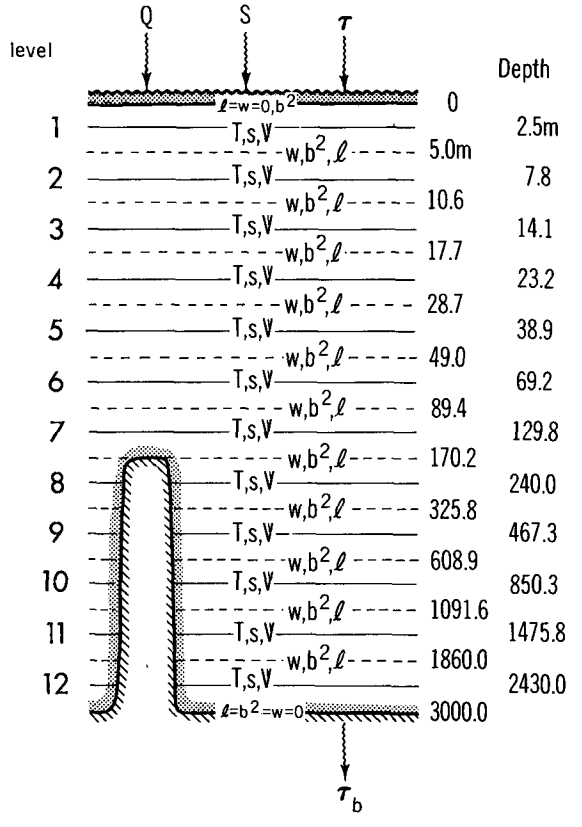

FIG. 1. A schematic diagram of the vertical resolution along with the placement of the variables.

e. *Initial conditions*

The A-physics version was initialized with climatological temperature and salinity (Levitus 1982) and with currents set to zero. Monthly averaged climatological winds (Hellerman and Rosenstein 1983) and SST (Levitus 1982) were used to force the model for 6 years, by which time an equilibrium seasonal cycle was established in the upper ocean. After this spinup stage, the model was then forced using observed 1982 and 1983 data as described in the following section. In the future, the model will be initialized using a "four-dimensional data assimilation scheme" currently being developed that will update the model with surface and subsurface oceanographic data (Derber 1987).

3. External forcings

In an ocean GCM, the usual procedure to handle the surface heat flux is to prescribe the SST and then calculate the downward heat flux using some vertical eddy diffusion coefficient. However, since SST is a field we are interested in simulating, this is not a viable choice. Instead, we must estimate the surface heat budget from available atmospheric and oceanic data. Although in the tropical oceans the wind field dictates the dynamics and therefore the patterns of SST, the amplitude is greatly influenced by the surface heat flux. Any systematic error in the heat flux would contaminate the SST values obtained by the model simulations. We feel this is important and hence we treat the computation of heat flux carefully and present it here in a rather complete form. Many researchers have tried to derive empirical equations relating the elements of standard marine meteorological observations to the heat budget at the ocean surface. All of the equations suffer from a lack of accurate measurements of the budget components. Our strategy for the radiation was to choose those formulas that were derived and verified by observations, limited as they are.

a. *Formulation of the surface heat flux components*

The net surface heat flux Q may be represented by

$$Q = Q_s - Q_u, \tag{3.1}$$

where Q_s is the downward flux of solar radiation and the net upward flux as used in (2.38) is

$$Q_u = Q_B + H_a + LE_a, \tag{3.2}$$

where Q_B is the net longwave (or "back") radiation emitted from the sea surface, H_a and E_a are the sensible and latent heat fluxes from the sea surface to the atmosphere, and L is the latent heat of vaporization. In Table 1, examples of each of the components of the surface heat flux are listed.

TABLE 1. Terms from surface heat flux (3.1) and (3.2) for December 1982. Units are in °C month^{-1}.

	150°E–180°	180°–150°W	150°–110°W	110°–80°W
		(20°–40°N)		
Q	−0.98	−1.39	−0.40	
Q_s	1.82	1.78	1.63	
Q_B	0.70	0.73	0.57	
H_a	0.29	0.36	0.07	
LE_a	1.80	2.09	1.38	
		(10°–20°N)		
Q	−0.55	−0.04	−0.07	
Q_s	3.47	3.36	3.15	
Q_B	0.70	0.72	0.71	
H_a	0.47	0.46	0.45	
LE_a	2.85	2.22	2.06	
		(2.5°–10°N)		
Q	1.29	1.15	0.95	1.60
Q_s	3.89	4.16	4.13	3.94
Q_B	0.62	0.84	0.92	0.85
H_a	0.28	0.43	0.45	0.28
LE_a	1.70	1.74	1.81	1.21
		(2.5°S–2.5°N)		
Q	1.98	1.74	1.54	2.38
Q_s	4.14	4.76	5.02	4.46
Q_B	0.64	0.89	1.15	0.87
H_a	0.20	0.34	0.42	0.21
LE_a	1.31	1.78	1.91	1.00
		(10°–2.5°S)		
Q	2.11	2.07	2.22	2.34
Q_s	4.37	5.00	5.57	5.00
Q_B	0.60	0.77	0.98	0.79
H_a	0.21	0.36	0.41	0.25
LE_a	1.41	1.80	1.96	1.32
		(20°–10°S)		
Q	2.50	1.72	2.20	
Q_s	5.02	5.06	5.60	
Q_B	0.66	0.78	0.91	
H_a	0.25	0.43	0.45	
LE_a	1.61	2.13	2.05	
		(40°–20°S)		
Q	2.91	2.84	2.90	
Q_s	5.09	4.76	4.76	
Q_B	0.72	0.68	0.69	
H_a	0.22	0.19	0.21	
LE_a	1.73	1.06	0.96	

Bunker (1976), Hastenrath and Lamb (1978), Weare et al. (1981), Esbensen and Kushnir (1981), and Hsuing (1986) have all discussed the difficulty in choosing appropriate formulas for Q over oceanic regions. This is especially the case for the radiative flux which, under generally cloudy skies, has many uncertainties associated with it.

1) SOLAR RADIATION

We have chosen to prescribe the solar radiation incident on the ocean under clear skies, after the *Smithsonian Meteorological Tables* (List 1958). The radiation at the top of the atmosphere is

$$Q_0 = \frac{J_0}{a^2} \cos z D_F(\phi, \lambda), \tag{3.3}$$

where the solar constant $J_0 = 1.35 \times 10^2$ J m^{-2} s^{-1}, a is the radius of the earth, and z is the zenith angle; cos$z$ is given by

$$\cos z = \sin\phi \sin\delta + \cos\phi \cos\delta \cos h, \tag{3.4}$$

where ϕ is latitude, δ the sun declination angle, and h the sun's hour angle. The fraction of daylight D_F is a function of latitude and longitude when diurnal effects are included. However, for this study it is a function of latitude only and is integrated over a full day. The direct component of solar radiation reaching the ocean surface is then attenuated by an atmospheric transmission coefficient τ as

$$Q_{\mathrm{DIR}} = Q_0 \tau^{\sec z}, \tag{3.5}$$

where $\tau = 0.7$. The diffuse sky radiation under cloudless conditions may be approximated by assuming that, when scattering of radiation occurs, half is scattered downward and half is scattered back. Thus we have

$$Q_{\mathrm{DIFF}} = [(1 - A_a)Q_0 - Q_{\mathrm{DIR}}]/2. \tag{3.6}$$

The water vapor plus ozone absorption A_a is taken to be 0.09. The total radiation reaching the surface under clear skies is then approximated by the sum of (3.5) and (3.6), i.e.,

$$Q_{\mathrm{TOT}} = Q_{\mathrm{DIR}} + Q_{\mathrm{DIFF}}. \tag{3.7}$$

Seckel and Beaudry (1973) made a harmonic representation of (3.6), the utility of which there is in general agreement. However, it is defined over a limited latitude band and could not be used with diurnal variation and so we chose to explicitly compute Q_{TOT}.

There are numerous empirical relations to predict the attenuation of solar radiation by clouds; we have chosen the formula derived by Reed (1977) and suggested by Simpson and Paulson (1979) to be in best agreement with observations:

$$Q_s = Q_{\mathrm{TOT}}(1 - 0.62C + 0.0019\beta)(1 - \alpha). \tag{3.8}$$

Here C is the fractional cloud cover, and β is the solar noon altitude in degrees and is computed by

$$\sin\beta = \sin\phi \sin[23.45 \sin(t - 82)] + \cos\phi \cos[23.45 \sin(t - 82)], \tag{3.9}$$

where t is the Julian day. The ocean surface albedo, α, is taken from Payne (1972), and these values agree very well with Simpson and Paulson's (1979) results. The variables, D_F, δ, h and β are all computed from

present day astronomy. The notion z, τ, t as defined here applies only to this section.

2) NET LONGWAVE RADIATION

The choice of an appropriate formula to calculate net longwave loss from the ocean surface under clear skies, Q_B, is as difficult as the choice for insolation. We have used the empirical relationship due to M. E. and T. G. Berliand (Budyko 1974), which includes an additional term due to air–sea temperature difference, i.e.,

$$Q_B = \epsilon\sigma T_s^4(0.39 - 0.05e_a^{1/2})(1 - BC) + 4\epsilon\sigma T_s^3(T_s - T_a), \quad (3.10)$$

where ϵ is the emissivity of the ocean (0.97), σ the Stefan–Boltzmann constant, e_a the atmospheric vapor pressure (mb), and T_s and T_a are the ocean and air temperature, respectively. The vapor pressure e_a can be expressed in terms of the saturation vapor pressure e_{sat} at the air temperature above the sea and relative humidity r, i.e.,

$$e_a \equiv re_{\text{sat}}(T_a), \quad (3.11)$$

where $e_{\text{sat}}(T_a)$ is computed using a polynomial approximation as a function of temperature (Lowe 1977).

Formulation (3.10) gave generally good agreement with the limited measurements of Simpson and Paulson (1979) for clear skies ($C = 0$). The modification due to cloudiness can have a considerable effect and yet the uncertainty as to the proper formulation is great. Following Reed (1976) and Simpson and Paulson (1979) we use a linear correction factor with $B = 0.8$.

3) SENSIBLE AND LATENT HEAT FLUX

The vertical flux of sensible and latent heat in (3.2) is parameterized by bulk turbulent transfer formulas

$$H_a = \rho_a c_p c_H |\mathbf{v}|(T_s - T_a) \quad (3.12)$$

$$E_a = \rho_a c_E |\mathbf{v}|[(e_{\text{sat}}(T_s) - re_{\text{sat}}(T_a)](0.622/p_a), \quad (3.13)$$

where $\rho_a = 1.2 \times 10^{-3}$ g cm^{-3} is the air density, $c_p = 1.005 \times 10^3$ J kg^{-1} K^{-1} is the specific heat capacity, $L = 2.501 \times 10^6$ J kg^{-1} and $C_H = C_E = 1.1 \times 10^{-3}$ are the turbulent exchange coefficients, $p_a = 1013$ mb is the surface air pressure, $|\mathbf{v}|$ is the wind magnitude, T_s is the ocean temperature at the top level of the model and represents SST, T_a represents the atmospheric temperature at 1000 mb, and $e_{\text{sat}}(T)$ is the saturation vapor pressure.

b. Parameterization of solar penetration

Although more than half of the insolation that enters the ocean is absorbed within the top half meter, the remaining fraction that penetrates can have a significant effect on the development of the thermal structure. Using the level 2.5 version of the Mellor–Yamada turbulence closure scheme for one dimension, both Martin (1985) and Simpson and Dickey (1981) studied the sensitivity due to solar flux divergence on upper-ocean thermal structure. Martin found the model simulations to be particularly sensitive to various optical water types, turbidity, during the spring and summer. Simpson and Dickey studied the effects of two irradiance parameterizations under various wind speeds and found that proper parameterization of downward irradiance is crucial for accurate predictions of upper ocean thermal structure. Following Paulson and Simpson (1977), the parameterization of absorption of downward irradiance is given by

$$I(z) = Q_s[R\exp(z/\zeta_1) + (1 - R)\exp(z/\zeta_2)], \quad (3.14)$$

where ζ_1 and ζ_2 are attenuation lengths and R is an empirical constant. Jerlov (1968) has classified oceanic water according to its optical properties. He defined five types of water varying from clear (Type I) to increasingly turbid (Type V). We used the values $R = 0.58$, $\zeta_1 = 0.35$ m, and $\zeta_2 = 23$ m, which correspond to Type I or clear. The divergence of downward irradiance may be written as

$$\frac{\partial I}{\partial z}, \quad (3.15)$$

which is included as a source term in (2.3). It should be noted that if the penetrative component of solar radiation is omitted, then all the heating takes place at the surface. This would be the same as if we were to include Q in (2.38) instead of Q_u and eliminate (3.15) from (2.3), which is a typical way of including the surface heat flux.

c. The momentum flux

The momentum flux is given by the wind stress,

$$\tau^\lambda = \rho_a c_D |\mathbf{v}|\mathbf{U}, \quad (3.16)$$

$$\tau^\phi = \rho_a c_D |\mathbf{v}|\mathbf{V}, \quad (3.17)$$

where c_D is the drag coefficient. The value of c_D is constant at 1.5×10^{-3}, which is in the middle range of values as determined by Bunker (1976). Here $\mathbf{U}$ and $\mathbf{V}$ represent the wind components.

d. The meteorological data

All of the atmospheric quantities, $\mathbf{U}$, $\mathbf{V}$, $|\mathbf{v}|$, T_a, and r, were obtained from the National Meteorological Center (NMC) 1000 mb analysis. This analysis is given every 12 h. The period covered was 0000 UTC 1 December 1981 to 1200 UTC 31 December 1983. For experiments that used monthly mean data, we simply averaged the 12 h analysis. The cloud cover, C, was

taken from the monthly mean climatological data from Esbensen and Kushnir (1981).

e. Discussion

Even though there are more up-to-date measurements for the solar constant, absorption, emissivity, and transmission coefficient than the ones used here, we chose not to incorporate them. This is because the empirical relationships used for the radiative terms were derived from the values that we stated earlier. Altering these constants would be tantamount to modifying the formulas, and unless the data used in deriving them were retrofitted, this is not advisable. Future plans do include making sensitivity studies on the effects of the cloud field on SST. We will contrast experiments that use heat flux based on climatological clouds with the "real" cloud field for 1982–83, based on a satellite-derived product.

As has been pointed out by Blanc (1985), the choice of transfer coefficient schemes is indeed perplexing. In this study we have circumvented this issue by using constant values. However, one of the schemes will be chosen and then tested, to see the effects of variable transfer coefficients on the model.

Using Reynolds' (1982) observed SSTs and the atmospheric data as previously described, we calculated monthly means of the various heat flux components. We then compared these to the atlas of Esbensen and Kushnir (1981) and found agreement within expected variability.

Although the degree of uncertainty in all of the above formulations is high, the patterns of heat exchange derived from the equations are probably realistic; however, absolute values and magnitude of gradients qualify only as approximations. For us, the final measure of success is how well the simulated SST agrees with observations.

4. The effects of subgrid-scale physics and atmospheric forcings

Two unique aspects of this modeling approach are the subgrid-scale (SGS) physics and the use of high frequency (every 12 hours) atmospheric forcings. In this section, therefore, we will focus our attention on these two aspects. We will compare the A-physics model forced by 12-hour and monthly mean data to the E-physics model also forced by 12-hour and monthly mean data. The discussion that follows will be limited to the tropical Pacific domain during the onset of the El Niño event. However, the basic conclusions appear to apply throughout the 25-month period during which we ran the ocean model.

a. Subgrid-scale variables

1) NONLINEAR VISCOSITY

Haney and Wright (1975) have shown that when a constant coefficient of lateral eddy viscosity A_M is used in ocean circulation models, a false computational spatial oscillation is generated in the western boundary region if A_M is smaller than a critical value. A realistic value of A_M in the open ocean may be more than an order of magnitude smaller than where shears or velocity gradients are large, e.g., the western boundary regions. Figure 2 shows the ratio of A_M for E-physics to A-physics at the first level (2.5 m), i.e., $(A_M)_E/(A_M)_A$, where $(A_M)_E$ is computed from (2.26) and $(A_M)_A = 10^8$ cm^2 s^{-1}. We can see that the nonlinear eddy viscosity coefficients are sensitive to the spatial scales of motion and therefore are relatively small in the open ocean [$\approx$2 orders of magnitude less than $(A_M)_A$], where the scales of motion are comparatively large, and are relatively large ($\approx$ unity) in regions where the scales are comparatively small. Since $(A_M)_E$ is proportional to the local deformation field, the shaded areas of Fig. 2 correspond to regions where the deformation or variability is large. It is interesting to compare this pattern with the global mesoscale sea height variability measured by the SEASAT altimeter as taken from Cheney and Marsh (1983). Since the satellite map illustrates the large-scale variability patterns due to current systems, it may be compared with the model's results in Fig. 2. We can see a fairly good correlation in regions of high variability, such as the Agulhas Current south of Africa, the Falkland/Brazil Current off South America, the Antarctic Circumpolar Current, and the north equatorial current systems in both the Atlantic and the Pacific. The Kuroshio and Gulf Stream stand out as highly energetic systems in the altimeter data; however, the model seems to underestimate that variability, particularly as it extends out from the coast.

It is interesting to note in Fig. 2 that $(A_M)_E$ is larger, by a factor of 10, in the summer hemisphere than in the winter hemisphere. A possible explanation is the compensating effects of the vertical and horizontal mixings. The vertical mixing is more intense in the winter hemisphere, due to convective overturning, and this tends to reduce the horizontal variability.

It is hoped that by reducing the lateral eddy viscosity, more energetic and realistic grid-scale motions, due to nonlinear effects, may be allowed to develop. Results presented later (Fig. 10) will illustrate this point. Certainly the utility of nonlinear viscosity, permitting smaller and more realistic values of A_M in the open ocean without causing false computational spatial oscillations, which would occur when using a constant value of A_M, has been demonstrated.

2) TURBULENT KINETIC ENERGY

Figures 3 and 4 show the surface and vertical distributions of the TKE, b^2, as computed from (2.9).

A noticeable feature of Fig. 3 is the increased intensity of TKE at middle and high latitudes of the winter hemisphere. These values reflect the large mixing due to convection when the ocean surface is being cooled,

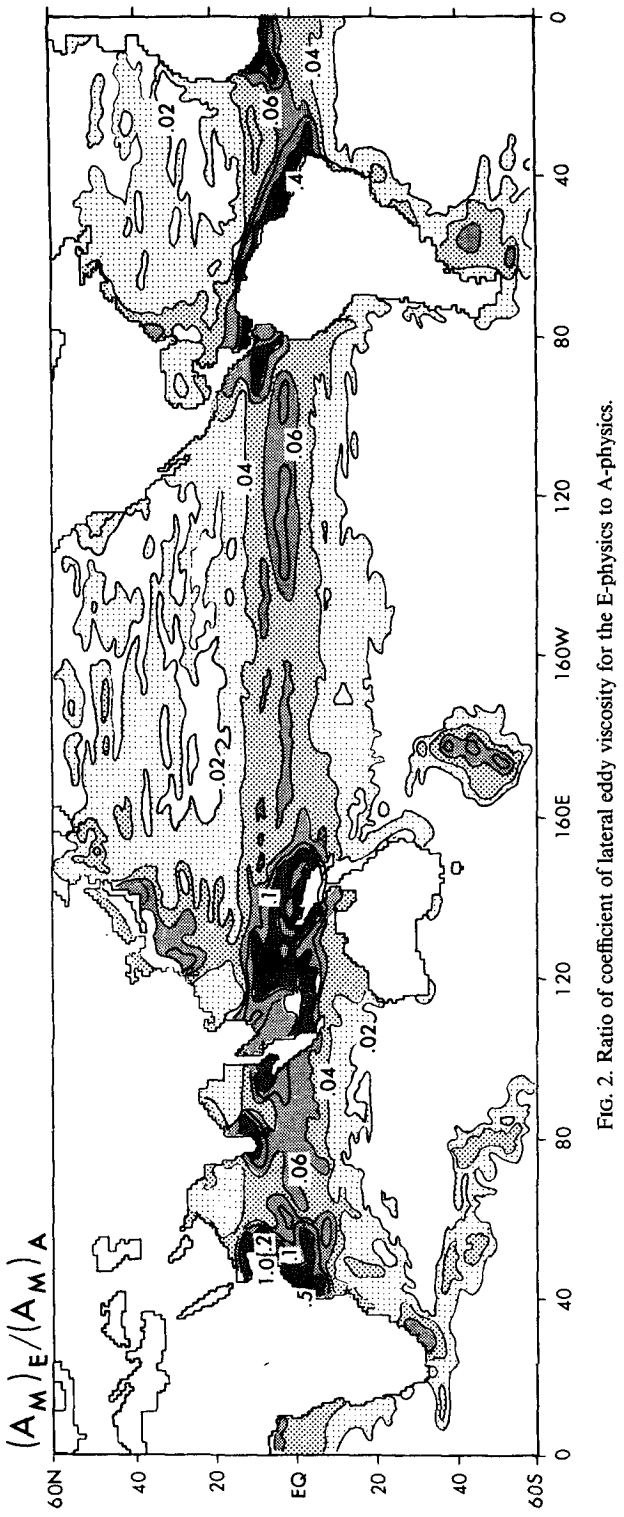

FIG. 2. Ratio of coefficient of lateral eddy viscosity for the E-physics to A-physics.

causing unstable stratification. Another obvious region of intense TKE is located over the Indian Ocean during the summertime, which is associated with the strong Somali jet in the atmosphere.

Figure 4 shows the vertical distribution of TKE along the equator for the Pacific basin during December 1982. This time period represents the end of the first phase of the 1982–83 El Niño. Associated with this event were exceptionally intense eastward currents along the equator, which were driven by strong westerly winds and were simulated by the model. As a result, we see in Fig. 4 that TKE is particularly large in the western Pacific, mixing momentum down into the ocean.

Figure 5 is a north–south vertical cross section along the dateline of the monthly mean vertical mixing coefficient K_H for December 1982. We can see that there are two prominent latitude bands with large values of K_H. One is the equatorial region where the TKE is high, as previously discussed and shown in Fig. 4. The second is the winter hemisphere where intense convective overturning is taking place.

Observations of turbulent dissipation by Crawford and Osborn (1981) gave the view that equatorial mixing had a strong equatorial maximum. As part of the TROPIC HEAT program, measurements of vertical profiles of turbulent dissipation were obtained at the equator and 140°W (Gregg et al. 1985; Moum and Caldwell 1985; Moum et al. 1986). Their findings were contrary to Crawford and Osborn (1981). Crawford and Osborn found that turbulent mixing does not have an obvious peak at the equator and that it is dominated by diurnal fluctuations. The earlier peak seems to be associated with the limitations of insufficient sampling. Examining Fig. 4 we see the spatial variability of TKE along the equator; i.e., between 160°E and 160°W the values are large but at 140°W, where the measurements were taken, they are small. A cross section at 180° (Fig. 5) shows an equatorial peak in TKE. However, if the section at 140°W were displayed we would not see it. Similarly, a comparison with the estimates of Gregg et al. (1985) for K_H shows that the model has similar values at 140°W, but at 180° the values are larger by a factor of 100. It may be noted that the model also contains temporal variability within the equatorial domain. These comparisons suggest that the limited observational data available at present may not be adequate for deriving parameterizations for numerical models that are applicable over the entire equatorial ocean. Although it is impossible to say if the TKE and the mixing coefficients are quantitatively correct, it does appear that qualitatively the values seem responsive to the physical mechanisms that cause them, i.e., winds, surface heating, and cooling.

b. The effects on the SST and surface currents

The impact that the SGS processes and the frequency of atmospheric forcings have on SST is displayed in

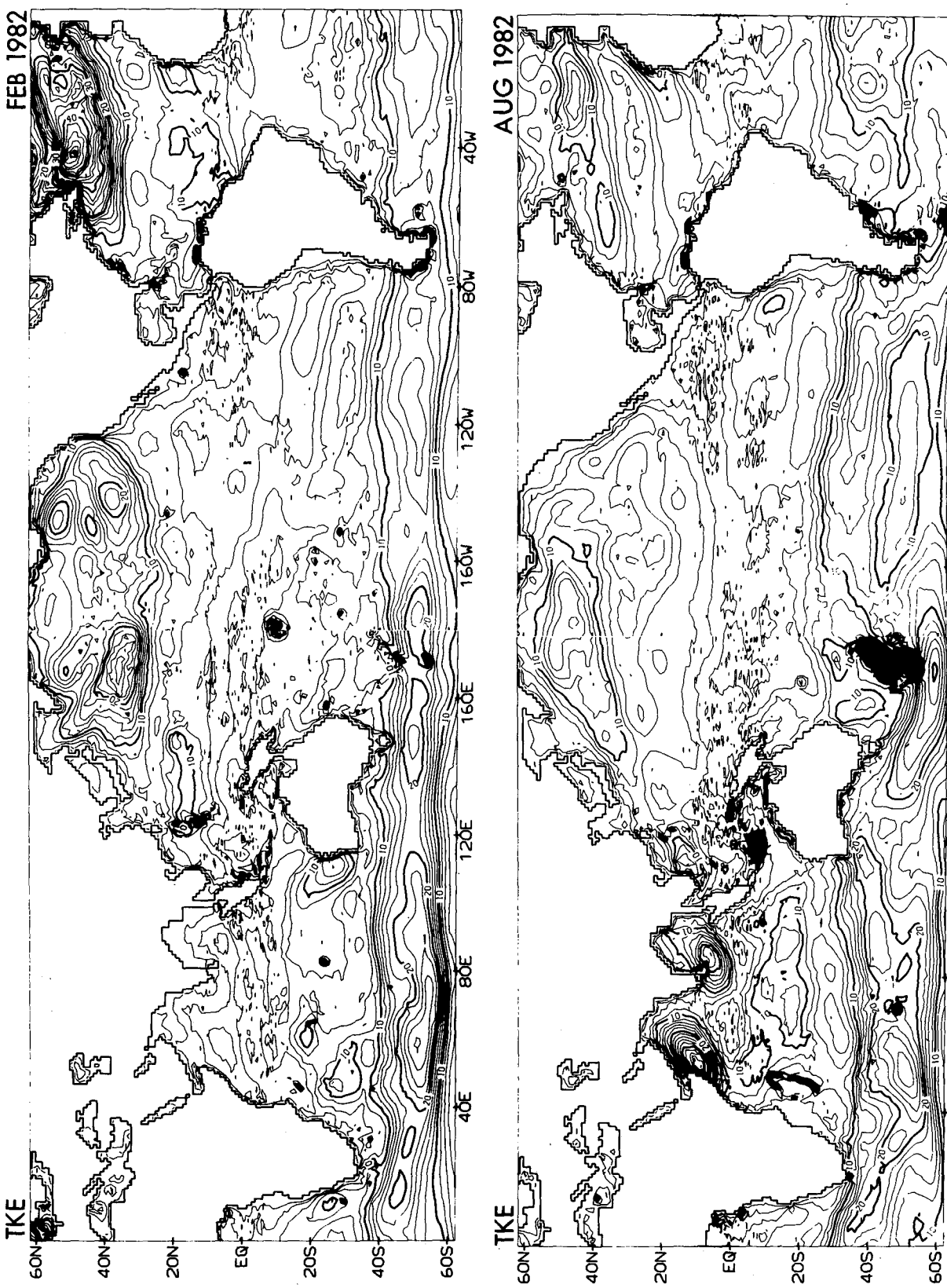

FIG. 3. Horizontal distribution of turbulence kinetic energy at the surface, computed from the E-12 model. Top panel: February 1982; bottom panel: August 1982. Units are $cm^2 s^{-2}$.

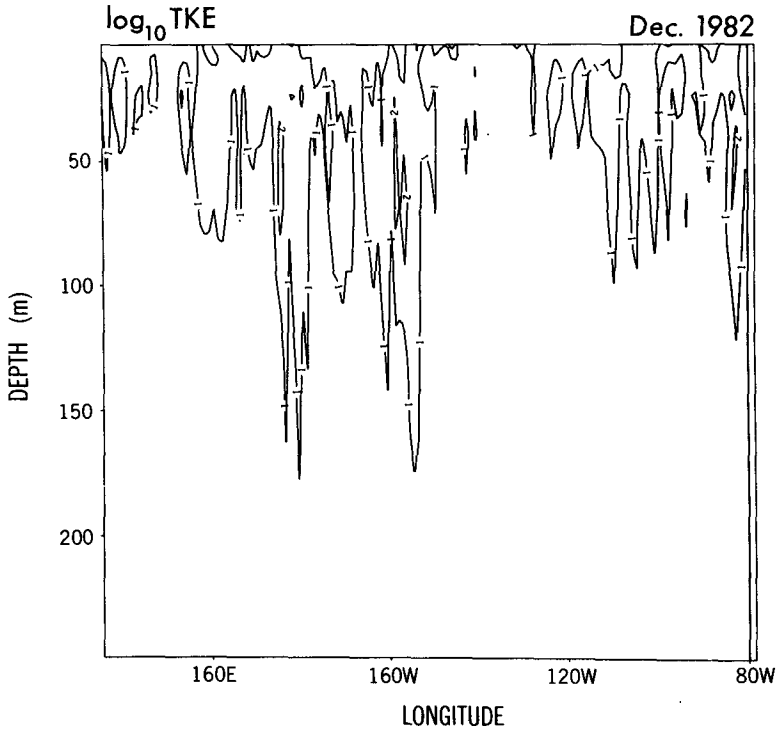

FIG. 4. Vertical distribution of turbulence kinetic energy along the equator for the Pacific basin. Units are $\log_{10}$ cm^2 s^{-2}.

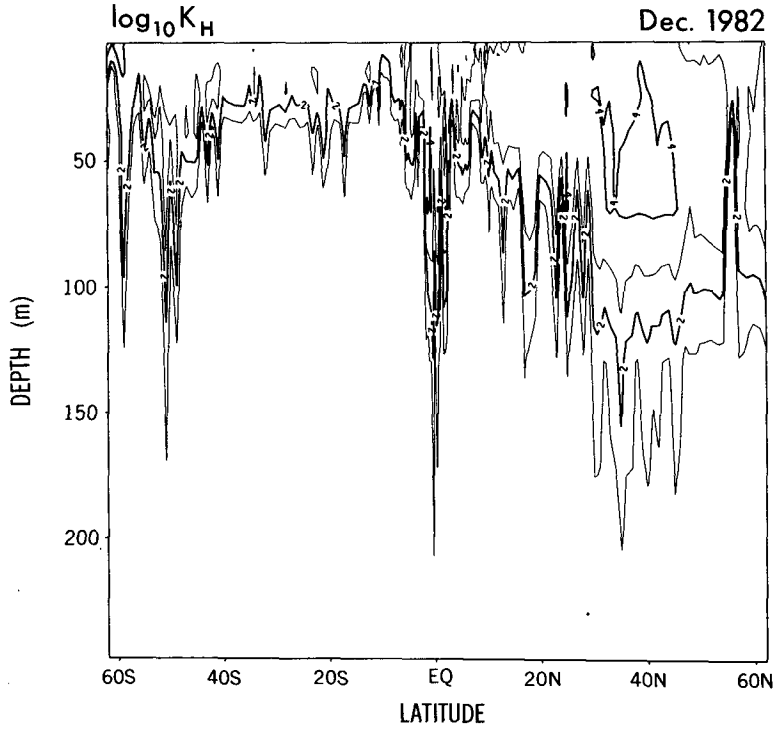

FIG. 5. North–south vertical cross sections at 180° for the vertical mixing coefficient. Units are $\log_{10}$ cm^2 s^{-1}.

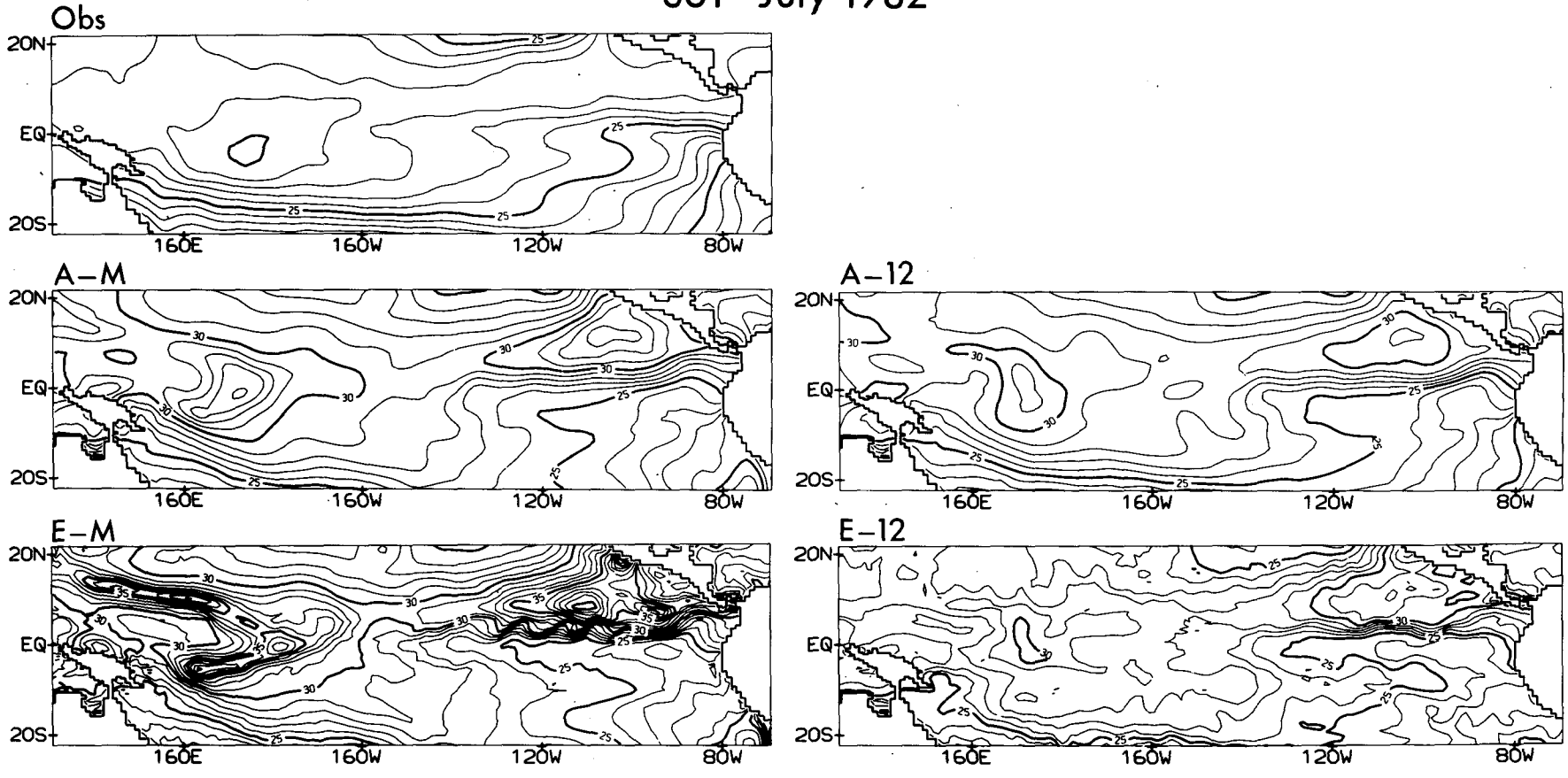

FIG. 6. Pacific basin SST for observation, A-M, A-12, E-M, and E-12 models. Contour interval 1°C.

Figs. 6 and 8. There are four model results: A-M, A-12, E-M, and E-12. The notations represent first the type of SGS physics and then the frequency of atmospheric forcings. For example, A-M denotes the A-physics with monthly mean forcings, and similarly, E-12 denotes the E-physics with 12-hourly atmospheric forcings. Monthly mean and 12-h data were chosen because these time periods represent the frequency at which analyzed products are currently available.

Figures 6 and 8 are monthly mean maps (averaged over every time step) of temperature and velocity, respectively, at the first layer (2.5 m) for July 1982 of the model simulation. For comparison, Fig. 6 also includes the observed SST field, which is based on Reynolds' (1982) analysis. Inspection of the SST fields leads to the following observations. 1) Both the A-M and the E-M models, which use monthly mean forcing, produce unrealistically warm temperatures off of New Guinea and Central America. 2) The A-12 and the E-12 models show quite reasonable simulation, although they, too, have the same regional bias as the monthly means but to a much lesser degree.

One possible explanation for this difference is that since the rate of evaporation, which is a large term in the heat budget, depends on wind speed, the evaporative flux is being underestimated. This would imply that in certain regions when the evaporative flux is large but the monthly mean wind speed is small, the wind variability must be taken into account so as not to underestimate the flux out of the ocean. Philander and Seigel (1984, hereafter referred to as PS), in their simulation of the 1982–83 El Niño, used monthly mean winds and parameterized the high-frequency wind fluctuations by requiring that the wind speed not be less than 4.8 m s^{-1}. Thus they avoided the excessively high surface temperatures. Although the SSTs in the PS model were too warm, they were somewhere between the A-M and the A-12 in Fig. 6.

Figure 7 shows the latent heat flux computed in two different ways. One way was to take the monthly mean values of each of the variables and calculate the flux, i.e.,

$$\bar{E}_a^{(1)} \propto \overline{|\mathbf{v}|} \cdot [e_{\text{sat}}(\bar{T}_s) - \bar{r}e_{\text{sat}}(\bar{T}_a)],$$

in Eq. (3.3), where $\overline{(\ )}$ is the monthly average. An-

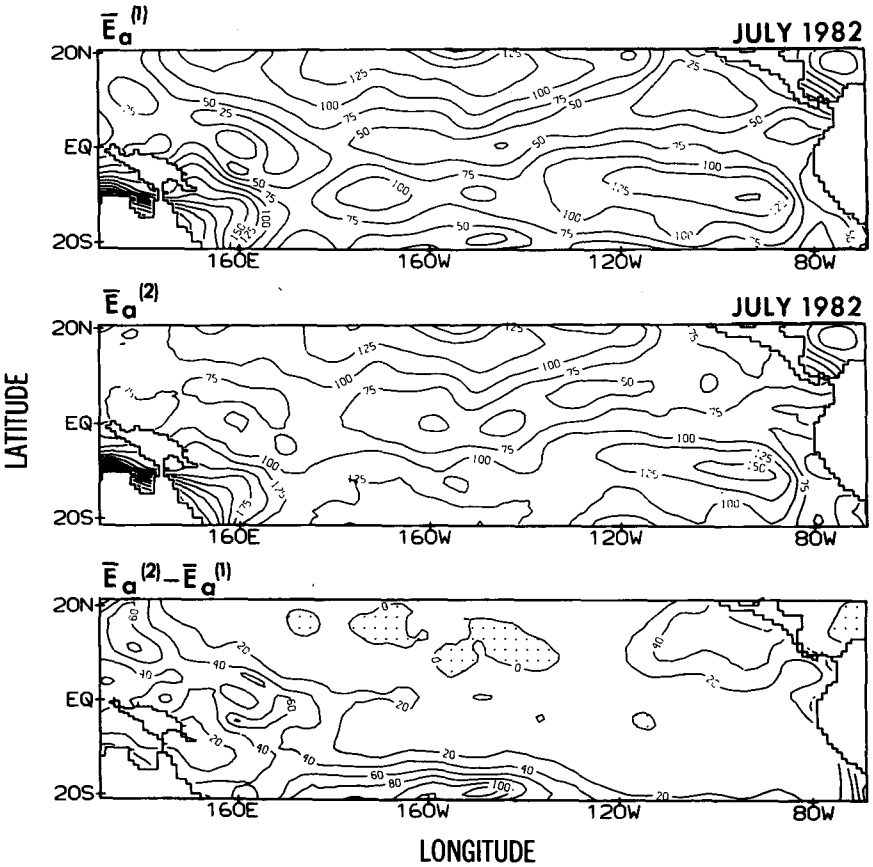

FIG. 7. Latent heat flux for (top) $E_a^{(1)}$ and (middle) $E_a^{(2)}$. Contour interval is 25 W m^{-2}. The bottom is the difference. Contour interval is 20 W m^{-2}.

other way is to use the 12-hourly data to compute the flux and then average, i.e.,

$$\bar{E}_a^{(2)} \propto \overline{|\mathbf{v}| \cdot [e_{\text{sat}}(T_s) - re_{\text{sat}}(T_a)]}.$$

The bottom panel in Fig. 7 shows the difference, i.e., $(\bar{E}_a^{(2)} - \bar{E}_a^{(1)})$, and we see in the two regions where the model had excessively warm SSTs, a corresponding underestimate of the evaporative flux. Esbensen and Reynolds (1981) distinguished these two methods of calculating heat flux by the *classical method* $(E_a^{(1)})$ and the *sampling method* $(E_a^{(2)})$. They concluded that monthly averaged values, as in the classical method, may be used to compute latent heat. However, it would appear from Fig. 7 that within the tropical region there must be some degree of variability for there to be such large differences between the two methods. Therefore, the sampling method seems more appropriate.

To further elucidate this point, another experiment was run with the A-physics in which the 12-hourly wind forcing was used to compute stress only but monthly mean values were used to compute the heat flux. In this run (not shown here), the hot spots are still present, indicating the need for high frequency winds to represent the evaporation properly. Other possible contributors to the error in heat flux are use of climatological clouds in the radiation and use of constant values for exchange coefficients, which are particularly sensitive to high wind speeds, and perhaps, the neglect of diurnal variation. The PS model and other simulations have used cruder approximations to the heat flux and yet have obtained quite reasonable results, primarily because of the equatorial ocean response to the wind field. However, close examination reveals large errors in the SST field, and so, if the concern is to produce a good SST product, one must treat not only the wind field but also the surface heat flux carefully.

Figure 8 depicts the monthly mean near-surface current (2.5 m depth) for July 1982. These particular figures show that the South Equatorial Current is dominant in the eastern Pacific and that the North Equatorial Counter Current starts to emerge at the far eastern basin. Overall, the patterns are similar within the same physics. It is noteworthy that the magnitude of the surface current vector is smallest in the E-12 model. This is because the E-physics together with the 12 hour forcings generates TKE (as shown in Fig. 3) and momentum is mixed down to subsurface layers.

The overall SST and surface current patterns between the two different physics appear quite similar, indicating the dominance of the wind forcing. However, the amplitudes are different between the A- and the E-physics, indicating the effect of the mixing parameterization and surface heat flux.

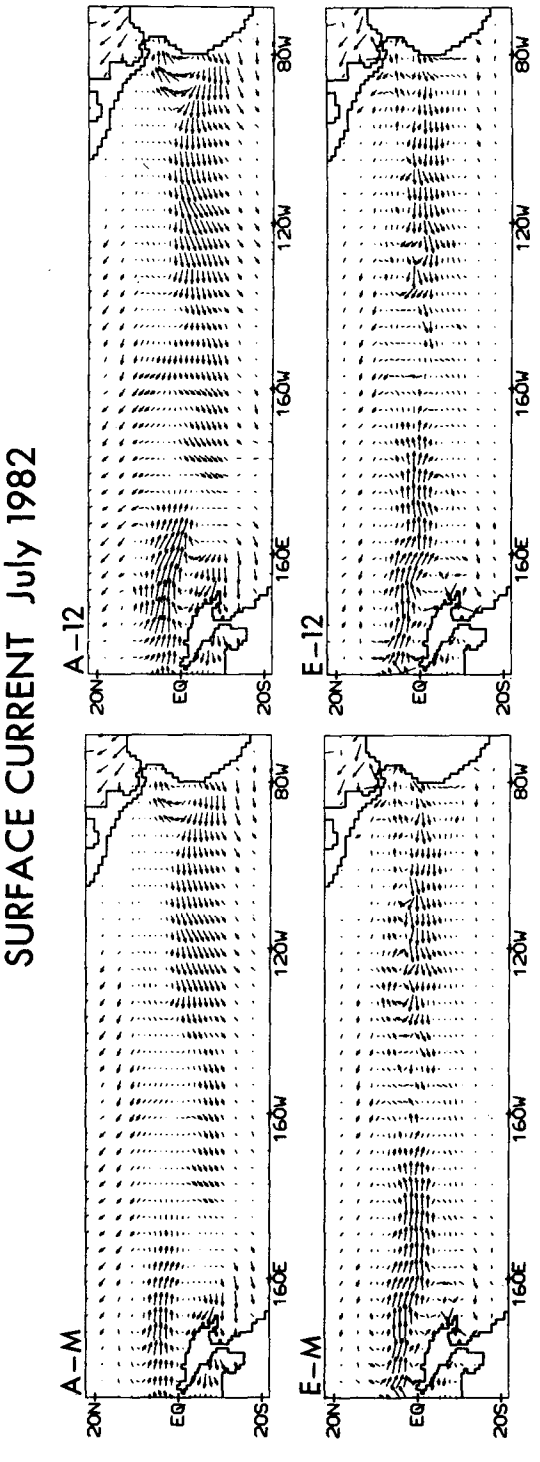

FIG. 8. Surface velocity vectors for the A-M, A-12, E-M, and E-12 models.

c. The effects on the thermal and current structure

The impact of the SGS processes and the frequency of atmospheric forcings on the vertical temperature and

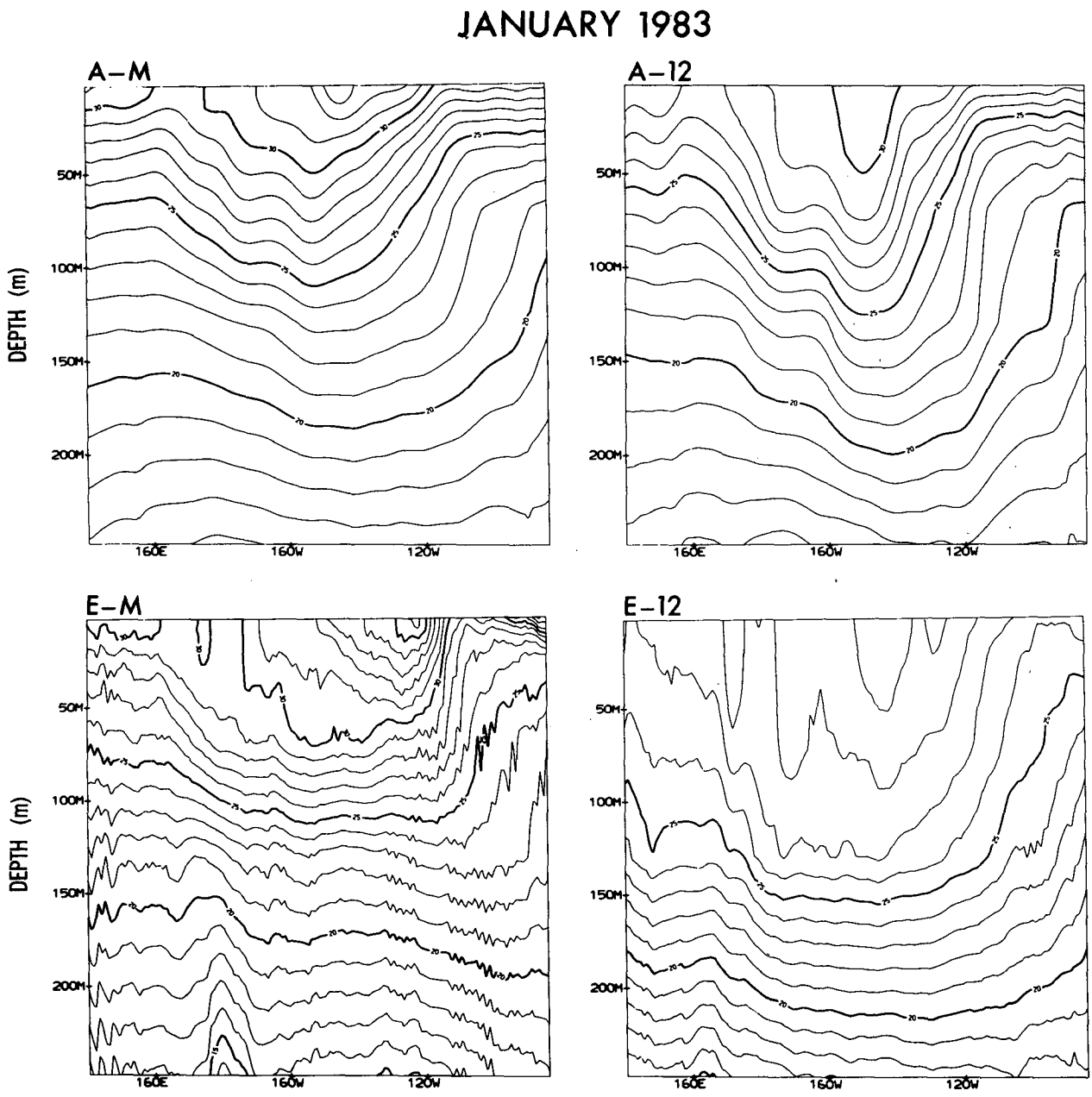

FIG. 9. Monthly mean zonal sections along the equator for temperature (°C) for the A-M, A-12, E-M and E-12 models.

current distribution is displayed in Figs. 9 and 10. Once again, the four model results are shown for temperature and velocity.

Figure 9 is a longitude–depth section of the monthly mean thermal structure along the equator for the Pacific in January 1983. First, it is remarked how evenly stratified all the model simulations are, none of which capture the tight temperature gradient associated with the thermocline. This suggests that the model's vertical resolution below 100 m is not sufficient. Apart from this drawback, it may be recognized in Fig. 9 that there are substantial differences in the slope and depth of the isotherms among the four models.

By January 1983, the El Niño event is well underway, so that the slope of the thermocline west of 160°W has reversed and slopes downward to the east (see PS). This tendency is displayed in all four models. The basic subsurface structure between A-M and A-12 is similar, indicating that the effect of the 12-hour wind forcing was to better represent the surface heat flux, as has been discussed, thus giving cooler near-surface temperatures. The E-M case is not very different from the

A-M and A-12 cases below 50 m, apart from the noise. Above 50 m the temperatures are even warmer than that of the A-M case. The explanation for this is that, even with the poor surface heat flux, there is always mixing with the constant mixing coefficients of the A-physics, and so heat is mixed below, whereas with E-physics the mixing coefficients are determined as functions of TKE. The very buoyant surface layer, which is formed from the monthly surface heat flux, retards the generation of turbulence and hence there is very little mixing. This leads to the excessively high temperatures, which will continue to increase until they come into equilibrium with the heat flux.

The E-12 model is markedly different from the others. One noticeable feature is how well mixed the temperature is, indicating that with proper boundary conditions the E-physics can be quite effective. We can also see that both the 20° and 25° isotherms are 50 m deeper than the other three models. The tighter temperature gradient below 100 m, the steeper downward slope of the thermocline, the deeper mixed layer, and cooler temperatures all distinguish the E-12 from the other three models, and qualitatively, it agrees better with observations.

Figure 10 shows time–depth diagrams of zonal current for the four models at 95°W and the equator for 1982. The shaded regions indicate westward flow. Once again, we see that the difference between A-M and A-12 is primarily near the surface, where the currents are somewhat stronger; otherwise they are close. However, when comparing A to E the difference in the strength of the surface currents and the equatorial undercurrent is apparent. It is evident that the zonal momentum balance is very sensitive to the parameterization of frictional processes adopted in the model. One advantage of choosing the turbulence closure scheme is that it accounts for mixing over multiple turbulent regimes, as is the case along the equator. The E-physics models, although better than the A-physics models, underestimate the strength of the undercurrent. A possible explanation for this may be that the vertical friction may be too strong and penetrating too deep. This could lead to too much dissipation of zonal momentum in the mixed layer and upper thermocline. Following Galperin et al. (1988) we limited the master length scale [Eq. (2.10)] in stably stratified flows according to

$$l \leq 0.53b/N, \tag{4.1}$$

where

$$N = \left(g \frac{\partial \rho}{\partial z}\right)^{1/2}$$

is the Brunt–Väisälä frequency. This limitation reflects the effects of stable stratification on the size of turbulent eddies. Preliminary experiments incorporating this limitation on l show that TKE has a sharp cutoff between turbulent regimes, thus controlling the leakage of vertical friction through the upper thermocline. This results in a less diffuse thermocline, and the strength of the undercurrent is increased by 50%. Consistent with these results, Philander and Pacanowski (1980) found that by reducing the coefficient of vertical eddy viscosity the speed of the equatorial undercurrent became more intense. The location of the core undercurrent might be better defined with increased vertical resolution between 75 and 150 m. Another aspect of the E-physics is that the nonlinear viscosity generates small values of horizontal eddy viscosity that allow for a more energetic flow field, which in turn may effect the vertical mixing. This interplay between horizontal and vertical mixing has also been discussed by Bryan and Lewis (1979).

d. The effects on mixed-layer depth

One-dimensional mixed-layer models have successfully simulated the observed evolution of SST and mixed-layer depth (MLD) at various weather ship stations (see Garwood 1979 for review). For these models the mixed-layer properties are determined primarily by local fluxes of heat and momentum. However, in regions such as the tropics, where the redistribution of heat due to the mean dynamics can be as important or more important than the local fluxes, the one-dimensional model fails. Hughes (1980), Pacanowski and Philander (1981), and Schopf and Cane (1983) have employed various turbulent models to include the behavior of the mixed layer in studies of the equatorial ocean. In this subsection, we will focus on the MLD from our model experiments.

Figures 11a and 11b display MLD in a time–longitude section along various latitude bands. We compare E-12 to A-12 for 1982 and also add the observed climatological MLD, after Levitus (1982), for comparison. The MLD is defined here as the depth at which the temperature difference from the top level exceeds 0.5°C.

Within the tropical band, (2.5°S–2.5°N), we see a very interesting feature in the climatological MLD, i.e., the unusually deep mixed layer in the central and western part of the Pacific compared to the very shallow mixed layer in the eastern Pacific. This basic equilibrium state is not well simulated by either model, although the E-12 model does considerably better than A-12, particularly for the 2.5°–10°N band. The reason for this inadequacy is not well understood since it is not clear why the surface turbulent boundary layer is so deep toward the western tropical Pacific. Garwood et al. (1985) stated that some physical process might be missing, namely, the usually neglected component of the Coriolis force on turbulent mixing. We are currently investigating this process. In any case it is important to reproduce this equilibrium mixed-layer depth because of its effects on heat content. Cane et al. (1986) hypothesize that heat content in the western Pacific plays a critical role in the ENSO cycle. We also

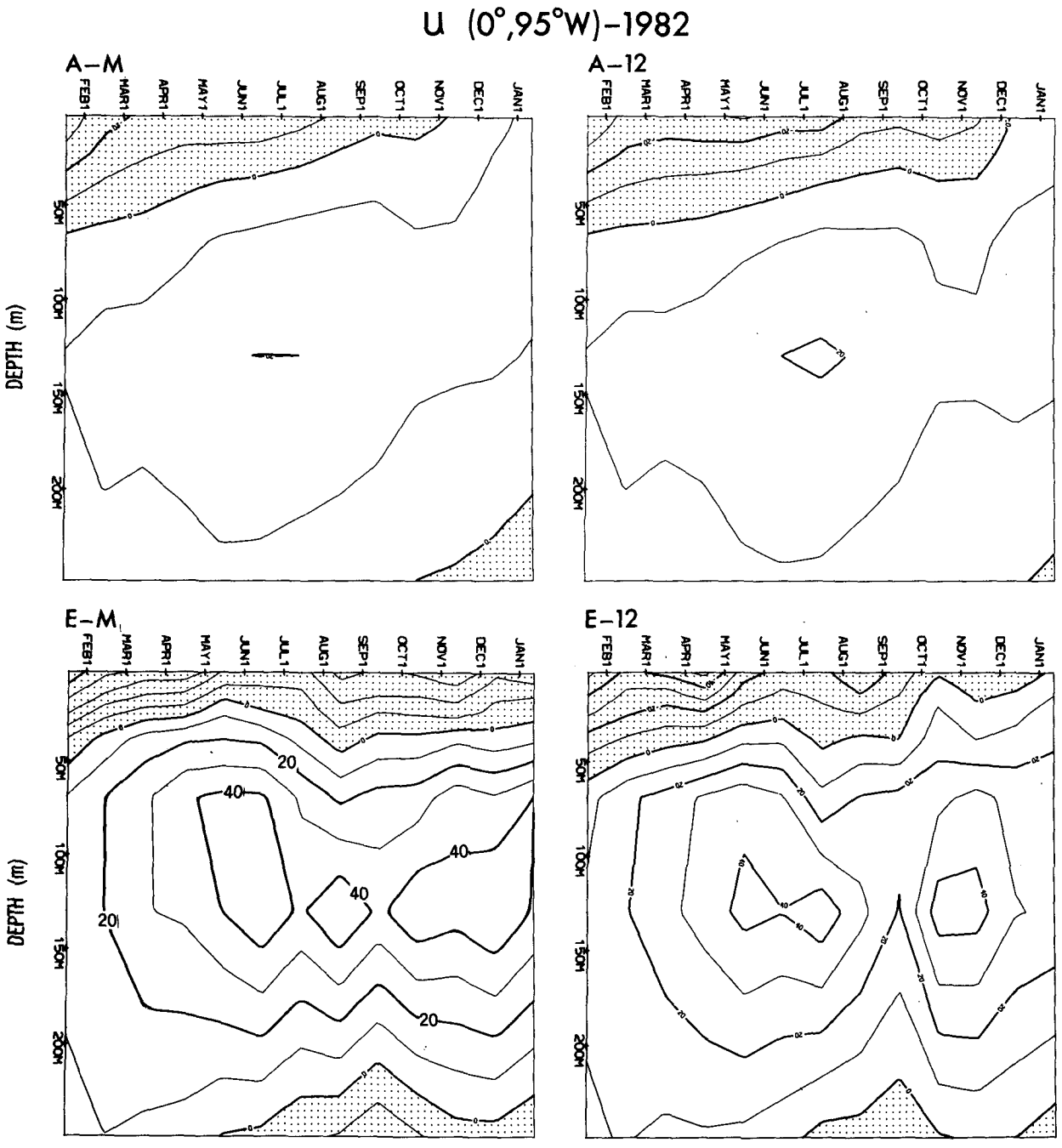

FIG. 10. Zonal velocity (contour interval = 10 cm s^{-1}) at the equator and 94.5°W during 1982 for the models A-M, A-12, E-M, E-12. Shaded areas denote westward flow.

notice the increased MLD in the 2.5°S–2.5°N band beginning in July and propagating eastward in E-12 and A-12. This is the signature from the strong westerly winds that occurred during this time and advected warm water eastward.

In Fig. 11b the seasonal cycle is evident. For the 10°–20°N band the E-12 model seems to be quite reasonable, with the phase and amplitude of the maximum and minimum in the right place. The MLD, within the 20°–40°N band, for the western region during the winter seems to be too deep for both E-12 and A-12. Because of the nonlinearity of convection, it could be that diurnal effects might be important for this region as well as the tropics.

The significant impact that high-frequency atmospheric forcing has on the simulation of MLD and, accordingly, on ocean forecasting was discussed previously by Miyakoda and Rosati (1984).

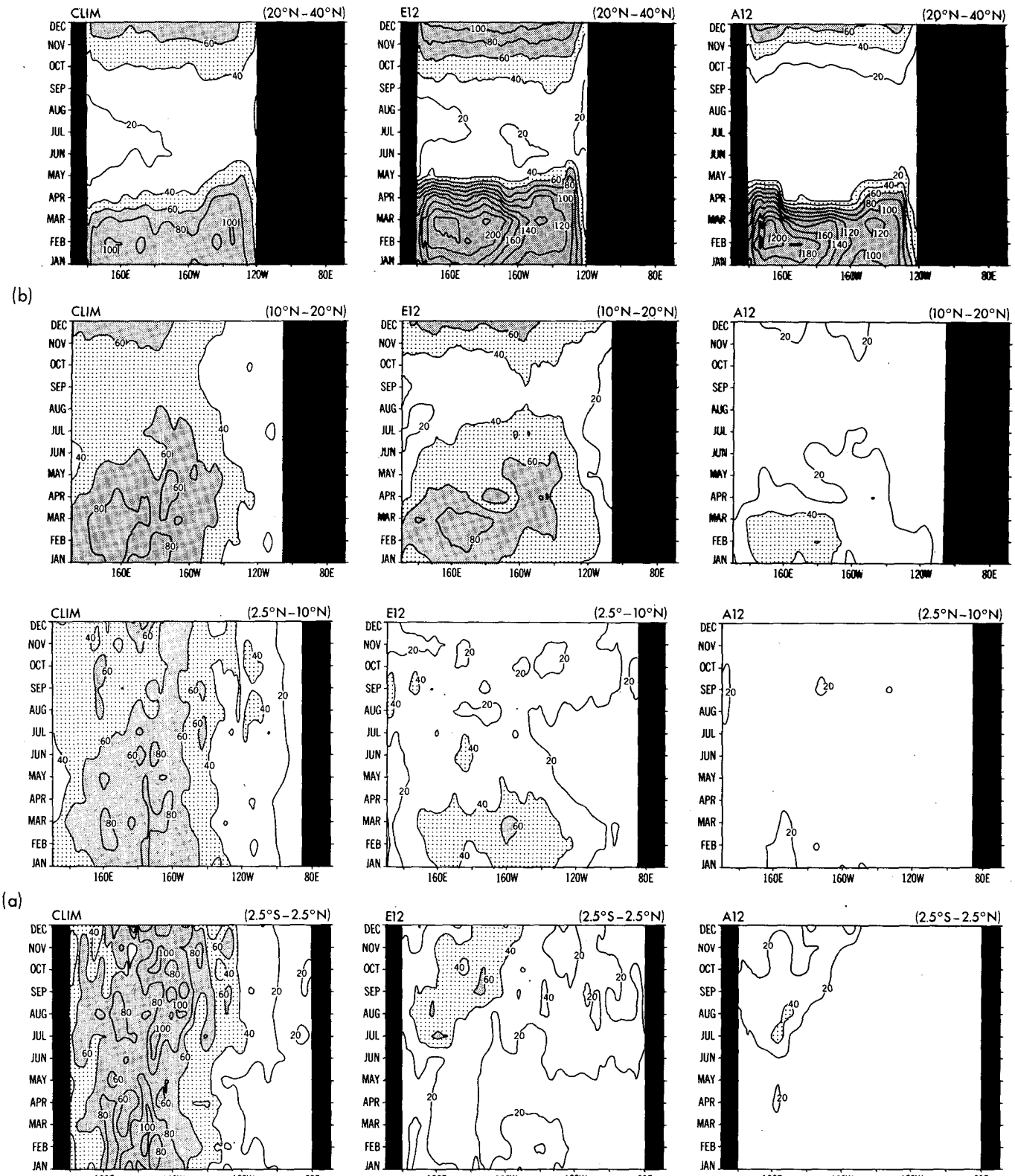

FIG. 11. (a) Mixed-layer depth (contour interval = 20 m) for latitude bands (bottom) 2.5°S–2.5°N and (top) 2.5°N–10°N. The left panels are climatology after Levitus (1982). The middle and right panels are the E-12 and A-12 models for 1982. (b) As in (a) but for 10°–20°N and 20°–40°N.

TABLE 2. Terms from temperature equation (2.6) for December 1982. Units are in °C month^{-1}.

	150°E–180°	180°E–150°W	150°–110°W	110°–80°W
		(20°N–40°N)		
$\partial_t T$	−0.61	−1.07	−0.71	
$-\partial_\lambda uT$	0.62	0.57	1.13	
$-\partial_\phi vT$	1.88	1.56	1.58	
$-\partial_z wT$	−2.44	−1.16	−2.84	
F_T	−0.42	−0.42	−0.32	
$\partial_z(-wT + v_T\partial_z T)$	−2.26	−2.46	−2.01	
$\partial_z I/\rho_0 c_p$	1.60	1.57	1.43	
		(10°N–20°N)		
$\partial_t T$	−1.53	−1.58	−1.36	
$-\partial_\lambda uT$	0.26	−1.60	−1.69	
$-\partial_\phi vT$	1.69	4.97	4.13	
$-\partial_z wT$	1.36	−2.97	−1.46	
F_T	−0.18	−0.12	−0.30	
$\partial_z(-wT + v_T\partial_z T)$	−5.16	−4.93	−5.22	
$\partial_z I/\rho_0 c_p$	3.06	2.96	2.77	
		(2.5°N–10°N)		
$\partial_t T$	1.83	−1.33	−0.73	0.11
$-\partial_\lambda uT$	−0.49	−4.41	1.90	2.67
$-\partial_\phi vT$	−4.57	−7.94	−7.36	−9.13
$-\partial_z wT$	4.79	12.70	6.05	6.75
F_T	0.10	−0.15	−0.12	−0.01
$\partial_z(-wT + v_T\partial_z T)$	−4.99	−5.35	−4.96	−3.64
$\partial_z I/\rho_0 c_p$	3.42	3.66	3.63	3.47
		(2.5°S–2.5°N)		
$\partial_t T$	−0.34	−0.49	1.06	0.93
$-\partial_\lambda uT$	4.31	−2.74	4.87	4.03
$-\partial_\phi vT$	−10.90	2.29	−8.29	−9.41
$-\partial_z wT$	6.46	−0.05	4.24	5.64
F_T	0.06	0.01	−0.01	0.14
$\partial_z(-wT + v_T\partial_z T)$	−3.88	−4.19	−4.17	−3.26
$\partial_z I/\rho_0 c_p$	3.64	4.18	4.41	3.92
		(10°S–2.5°S)		
$\partial_t T$	0.24	0.11	0.63	0.69
$-\partial_\lambda uT$	−4.46	−1.21	2.56	0.89
$-\partial_\phi vT$	3.22	−2.72	−0.65	−0.13
$-\partial_z wT$	1.08	3.91	−1.86	−1.05
F_T	0.07	−0.06	−0.09	0.18
$\partial_z(-wT + v_T\partial_z T)$	−3.43	−4.28	−4.31	−3.25
$\partial_z I/\rho_0 c_p$	3.82	4.40	4.90	4.23
		(20°S–10°S)		
$\partial_t T$	1.30	0.42	0.81	
$-\partial_\lambda uT$	2.42	−1.99	0.23	
$-\partial_\phi vT$	−5.40	−2.33	1.25	
$-\partial_z wT$	3.15	4.47	−1.26	
F_T	0.30	0.34	0.19	
$\partial_z(-wT + v_T\partial_z T)$	−3.28	−4.17	−4.32	
$\partial_z I/\rho_0 c_p$	4.41	4.45	4.93	
		(40°S–20°S)		
$\partial_t T$	1.42	1.17	1.36	
$-\partial_\lambda uT$	0.49	0.30	−0.10	
$-\partial_\phi vT$	1.84	1.11	1.85	
$-\partial_z wT$	−2.16	−1.40	−1.59	
F_T	0.65	0.62	0.67	
$\partial_z(-wT + v_T\partial_z T)$	−3.21	−3.04	−2.98	
$\partial_z I/\rho_0 c_p$	4.46	4.19	4.19	

TABLE 3. Terms from TKE (2.9) for December 1982. Units are $cm^2\ s^{-3}$ ($\times 10^4$) and $cm^2\ s^{-1}$ for K_H.

	150°E–180°	180°–150°W	150°W–110°W	110°W–80°W
		(20°N–40°N)		
$\partial_t b^2$	−0.06	0.01	−0.01	
$\partial_z(K_b \partial_z b^2)$	320.00	312.00	227.00	
$2\overline{wu}\partial_z u + 2\overline{wv}\partial_z v$	99.00	142.00	111.00	
$\partial g w \rho/\rho_0$	6.70	8.33	3.06	
$\mathcal{L}(b^2)$	0.06	0.06	0.06	
F_b	0.00	−0.00	0.00	
$2b^3/B_1 l$	430.00	463.00	340.00	
K_H	2900.00	3150.00	2060.00	
		(10°N–20°N)		
$\partial_t b^2$	0.24	−0.16	0.61	
$\partial_z(K_b \partial_z b^2)$	840.00	3050.00	1670.00	
$2\overline{wu}\partial_z u + 2\overline{wv}\partial_z v$	210.00	240.00	263.00	
$\partial g w \rho/\rho_0$	−1.30	4.81	−7.71	
$\mathcal{L}(b^2)$	0.39	0.48	0.26	
F_b	0.03	−0.04	0.26	
$2b^3/B_1 l$	1050.00	3290.00	1930.00	
K_H	1610.00	1610.00	1230.00	
		(2.5°N–10°N)		
$\partial_t b^2$	−0.12	−0.21	−0.12	0.13
$\partial_z(K_b \partial_z b^2)$	3650.00	8480.00	5520.00	6930.00
$2\overline{wu}\partial_z u + 2\overline{wv}\partial_z v$	237.00	169.00	137.00	104.00
$\partial g w \rho/\rho_0$	−13.90	−10.50	−9.52	−12.2
$\mathcal{L}(b^2)$	0.25	0.48	0.31	0.19
F_b	−0.00	−0.01	−0.00	0.03
$2b^3/B_1 l$	3870.00	8640.00	5650.00	7020.00
K_H	729.00	938.00	819.00	376.00
		(2.5°S–2.5°N)		
$\partial_t b^2$	−0.79	0.01	0.17	0.05
$\partial_z(K_b \partial_z b^2)$	8520.00	1320.00	3950.00	3590.00
$2\overline{wu}\partial_z u + 2\overline{wv}\partial_z v$	79.50	52.20	56.70	70.30
$\partial g w \rho/\rho_0$	−8.80	−1.96	−3.98	−10.80
$\mathcal{L}(b^2)$	0.11	0.12	0.07	0.05
F_b	−0.00	0.02	0.01	0.01
$2b^3/B_1 l$	8590.00	1370.00	4010.00	3650.00
K_H	711.00	1620.00	779.00	259.00
		(10°S–2.5°S)		
$\partial_t b^2$	−0.80	−0.01	−0.03	0.04
$\partial_z(K_b \partial_z b^2)$	45000.00	5660.00	2100.00	922.00
$2\overline{wu}\partial_z u + 2\overline{wv}\partial_z v$	86.10	84.40	68.80	75.90
$\partial g w \rho/\rho_0$	−8.50	−6.80	−5.82	−5.10
$\mathcal{L}(b^2)$	0.12	0.16	0.08	0.04
F_b	−0.00	−0.00	0.02	−0.00
$2b^3/B_1 l$	45100.00	5740.00	2170.00	992.00
K_H	429.00	782.00	654.00	453.00
		(20°S–10°S)		
$\partial_t b^2$	−0.00	−0.17	−0.00	
$\partial_z(K_b \partial_z b^2)$	2130.00	2190.00	1180.00	
$2\overline{wu}\partial_z u + 2\overline{wv}\partial_z v$	97.40	117.00	142.00	
$\partial g w \rho/\rho_0$	−5.69	−4.79	−5.07	
$\mathcal{L}(b^2)$	0.00	0.05	0.02	
F_b	0.00	−0.01	−0.00	
$2b^3/B_1 l$	2220.00	2300.00	1320.00	
K_H	310.00	539.00	494.00	

TABLE 3. (*Continued*)

	150°E–180°	180°–150°W	150°W–110°W	110°W–80°W
		(40°S–20°S)		
$\partial_t b^2$	0.00	−0.00	−0.05	
$\partial_z(K_b \partial_z b^2)$	262.00	218.00	380.00	
$2\overline{wu}\partial_z u + 2\overline{wv}\partial_z v$	308.00	200.00	204.00	
$\partial g w \rho / \rho_0$	−5.76	−6.37	−6.04	
$\mathcal{L}(b^2)$	0.00	0.00	0.02	
F_b	−0.00	0.00	0.00	
$2b^3/B_1 l$	565.00	411.00	578.00	
K_H	361.00	320.00	318.00	

5. Near-surface heat balance

In order to gain some insight into the heat budget of the model, we examine the balance of terms for the equations of surface heat flux, temperature, and TKE. Each term of the equations is averaged over the top four levels (28.7 m) and monthly mean values are computed. These values are then averaged over various subdivisions. By way of example, the Pacific Ocean and December 1982 were chosen; this corresponds to the mature phase of the El Niño. A single month, as opposed to an annual mean, was selected to show the seasonal variation within selected latitude bands. Positive (negative) values represent a net gain (loss) of the quantity.

a. Surface heat flux balance

Table 1 contains the values of each term of the surface heat flux, Q, in (3.1) and (3.2). So that the units (°C month^{-1}) are consistent with the temperature equation, all of the surface heat flux terms are divided by $\rho_0 c_p$. Looking at the latitudes poleward of 10°, the Northern Hemisphere winter and the Southern Hemisphere summer are quite discernible in Q. The primary component for this feature is the shortwave radiation, Q_s, which decreases to the north and increases to the south. The second most important term is the latent heat flux, LE_a. This term is very dependent on wind speed and so its seasonal fluctuations are a function of wind; this is particularly evident in the 20°–40°N band. The third largest term is the longwave radiation, Q_B, which is dependent on SST and cloud cover. The smallest term, the sensible heat flux, H_a, is proportional to the air–sea temperature difference. When that difference is small, this term is very small; however, when the difference is large, as in 20°–40°N, H_a becomes more significant and can even change sign.

Within the tropical band (10°S–10°N), where heat is gained throughout the year, some interesting features may be noted. Unlike the 10°–40° bands, where the primary variation occurs meridionally, the 10°S–10°N band has its primary variance occurring zonally. From 150°E to 110°W, Q decreases because of the increase primarily in LE_a and Q_B, H_a. Within 110° to 80°W, however, we see a marked increase in Q and decreasing LE_a; this is associated with the colder SST in the east. Even though the dominant terms are Q_s and LE_a, their difference is of comparable magnitude to the other terms.

b. Thermal balance

Table 2 contains each of the terms of the temperature equation (2.3). Here again the seasonal variation is pronounced. The rate of change of temperature increases poleward of 2.5°N and decreases poleward of 2.5°S. Within these higher latitude bands, the dominant terms are vertical diffusion, $\partial_z(-\overline{wT} + \nu_T \partial_z T)$, a sink, and divergence of irradiance, $\partial_z I/\rho_0 c_p$, a source. Recalling from (2.38) that the top boundary condition for diffusion of temperature is Q_u, the net upward heat flux, we can see why this term is a net heat loss. For 20°–40°N (winter extratropics) we see that the vertical diffusion term is about half of the value for other latitude bands. The cause of this is that during December there is convective overturning in this band and heat is being diffused upward, and this would be a source of heat to the upper levels. The difference between diffusion and irradiance can be thought of as the surface heat flux and can be compared to Q from Table 1. Basically, the heat flux across the ocean surface is approximately equal to and hence usually determines the rate of change of temperature for latitudes off the equatorial region. This would imply that local one-dimensional mixed-layer processes govern these areas. This is evidenced by noting that the three-dimensional divergence of temperature, $-\partial_\lambda uT - \partial_\phi vT - \partial_z wT$, is relatively small, as is horizontal diffusion, F_T.

The tropical region is quite a different matter. Here, the divergence terms are much larger and the difference between the vertical diffusion and irradiance is smaller. Therefore, the balance is much more subtle, i.e.; we have small differences between large numbers. The rate of change in temperature is not only due to the surface heat flux but also to the three-dimensional divergence of temperature. Looking at 2.5°S–2.5°N we see that in the western region heat is lost and in the east there is a heat gain. This is because during December 1982

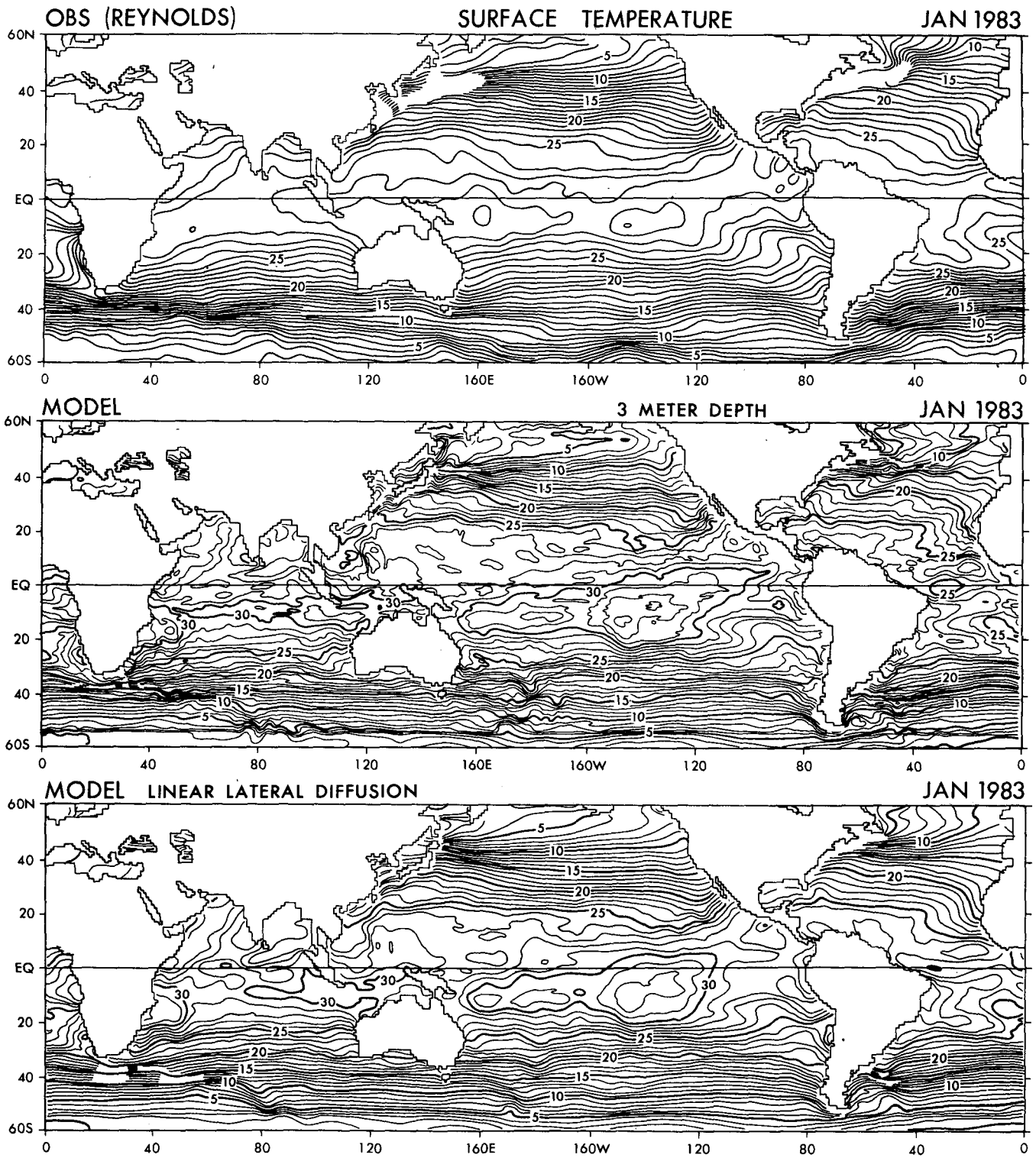

FIG. 12. Monthly mean maps of SST (°C).

the trade winds were relaxed and westerlies advected warm water eastward. This analysis shows that advection of heat during the 1982–83 El Niño contributed to the changes in the surface thermal structure. This is consistent with the findings of Reed (1983) for the 1972 El Niño. We also note that the meridional heat transport term $-\partial_\phi vT$ is the large term indicating poleward surface flow. Philander and Pacanowski (1986)

also found similar results for the Atlantic. They found that the rate of change in heat content south of 5°S is very similar in phase and amplitude to the surface heat flux. However between 5°S and 15°N, where the heat transport is northward, the divergence of the meridional heat transport is comparable in magnitude to the change in heat content.

c. *TKE balance*

We have seen that the vertical mixing processes are very important in determining the temperature structure. Since these processes are governed by the mixing coefficient K_H, we include an analysis of the TKE (2.9) in Table 3. For all latitude bands the TKE is dominated by turbulent vertical diffusion, $\partial_z(K_b\partial_z b^2)$, and dissipation, $-2b^3/B_1 l$. Once again, the reason the diffusion term is large is that the surface boundary condition (2.40), which is proportional to the friction velocity u_*, is contained within it. As with heat flux, the two largest terms are nearly equal and of opposite signs. This means that their difference is balanced by the next largest term, shear production, $-2\overline{wu}\partial_z u - 2\overline{wv}\partial_z v$, as well as by buoyancy production, $-2g\overline{w\rho}/\rho_0$. The advection term, $-\mathcal{L}(b^2)$, and the horizontal diffusion, F_b, of TKE are relatively insignificant. Within 20°–40°N we see that the buoyancy production term is positive. This is due to the wintertime negative surface heat flux creating unstable conditions and thus increasing production of TKE. The average value for K_H is about 500 $cm^2\ s^{-1}$, indicating that the top four levels are well mixed throughout the whole domain shown here.

6. Results of the numerical studies

In this section we will present a brief overview of some selected results from the E-12 model.

a. *Global SST*

Figure 12 displays the global SST patterns for observations as well as for two different model results for January 1983. The middle panel is the E-12 model and the increased small-scale features are readily discernible compared to observations. In order to investigate this point, we ran an experiment replacing the nonlinear lateral diffusion with the linear lateral diffusion from the A-physics model, seen in the lower panel. Notice that a much smoothr pattern emerged, showing the effects of the larger horizontal mixing. In both model results the anomalously high temperatures in the eastern Pacific, during the height of the El Niño, may be seen.

Figure 13 shows the SST difference field for the E-12 model minus the observations. Unshaded regions are areas where the differences are $\leq 1.0°$. The largest errors are in the western boundary region of the Kuroshio and Gulf Stream. Within the tropical Pacific

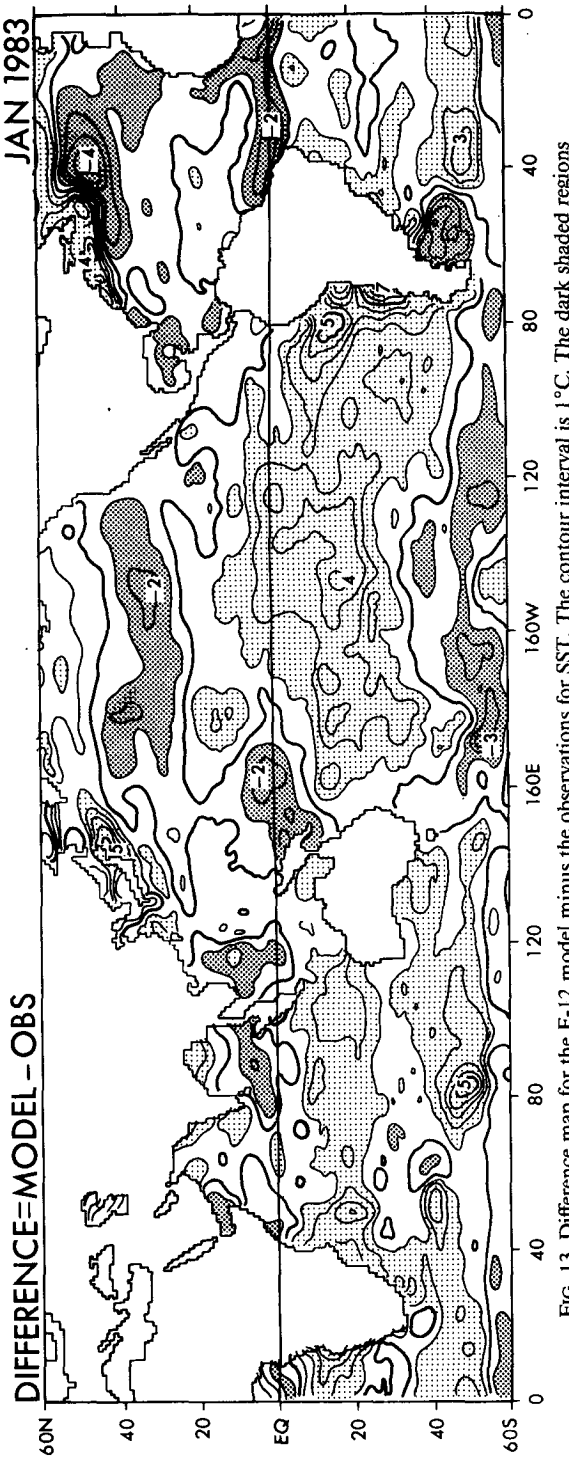

FIG. 13. Difference map for the E-12 model minus the observations for SST. The contour interval is 1°C. The dark shaded regions represent differences <1°C, and the light shaded regions represent differences >1°C.

the warm event was captured, but the model appears to have overestimated the temperature.

b. *Vertical structure of temperature and velocity*

Figures 14 and 15 are cross sections of temperature and zonal velocity along the equator at 95°W for 1982 and 1983. The upper figures are the model simulations and the lower figures are the observed values after Halpern (1987). The observations of Fig. 14 show the complex vertical structure of the evolution of heat content during the 1982–83 El Niño event at 95°W. We see the thermocline steadily deepening during 1982. In April and May 1983, we see a rise in SST rather than the continued deepening of the thermocline, and finally, in June 1983 we see the restoration to normal conditions (for a more extensive discussion see PS). Overall, the ability of the model to simulate these changes at the equator is demonstrated. Two serious flaws of the model are the lack of a well-defined thermocline and the inability for the isotherms to rise to the surface toward the end of 1983. The first discrepancy can possibly be attributed to incorrect initial conditions and the lack of vertical resolution. The second discrepancy, indicating the poor performance of the model in recovering from El Niño after July 1983, is related to the errors in the wind field.

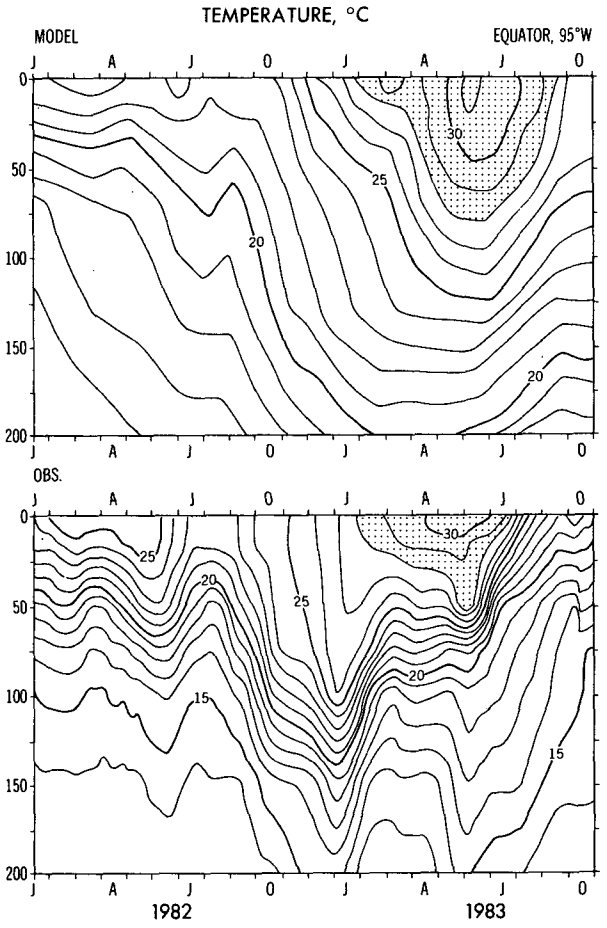

FIG. 14. Temperature (°C) at 95°W and the equator during 1982–83. Top: the E-12 model simulation. Bottom: observations after Halpern (1987). Shaded areas indicate values greater than 28°C.

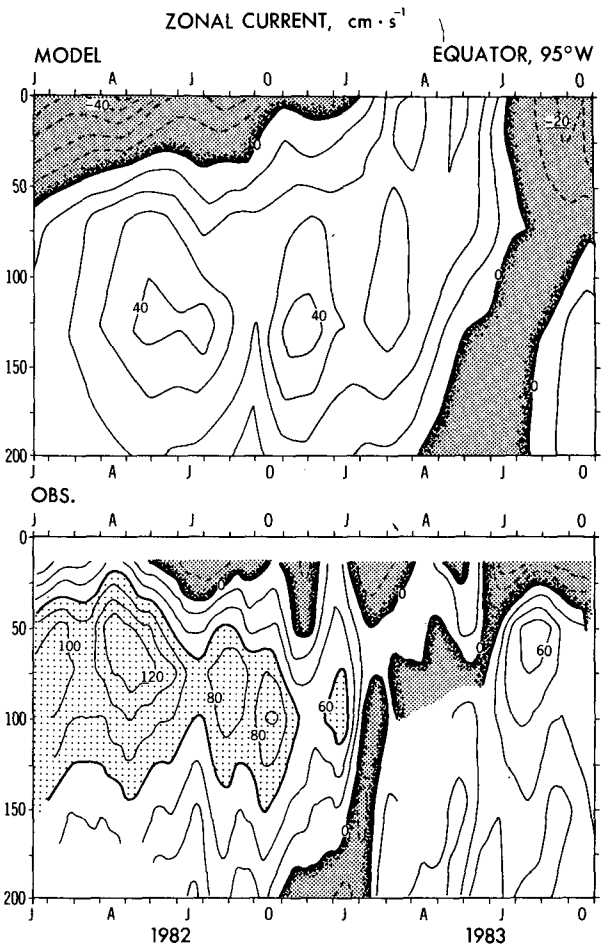

FIG. 15. As in Fig. 14 but for zonal velocity. Dark shading indicates westward flow.

In Fig. 15 the observations show a deceleration of the Equatorial Undercurrent during 1982, the appearance of an eastward jet during April–June 1983, and finally, normal conditions. Once again the model captures the gross features. However, the major shortcomings are a considerable underestimation of the Equatorial Undercurrent speed and a poor simulation of the phase of the return to normal.

7. Summary and conclusions

An ocean GCM has been constructed with an objective of simulating the upper-ocean thermal structure. Preliminary tests have been performed, using realistic atmospheric boundary forcing.

The model is global in domain with horizontal resolution of 1° longitude by 1° latitude but ⅓° latitudinal resolution within the 10°S–10°N equatorial band. It has 12 vertical levels and incorporates realistic bottom

topography. The SGS physics includes horizontal nonlinear eddy viscosity and the Mellor–Yamada level 2.5 turbulence closure scheme for vertical mixing. The atmospheric boundary forcing was the NMC analysis for the 1982–83 period. This time period was selected because it contained the El Niño and the simulation of this event would be a good test of the model.

Experiments were run comparing two versions of the model, A-physics and E-physics, and two different frequencies of forcing, 12 hour and monthly. Intercomparison with the different forcings on the same model reveals that the monthly mean forcing produces excessively high temperatures within the tropics due to the underestimation of the evaporative flux. This occurs in regions where the mean wind speed is small but the variability is large. This is evidenced by comparing the A-M model to the A-12 model and the E-M model to the E-12 model, where we see the improvement using the 12-hour forcing. Within the E-physics model another aspect of the forcing is manifest. The surface-layer mixing depends synoptically on the surface wind stress vector τ; however, the Ekman transport depends on τ^λ and τ^ϕ. For the E-physics case, monthly mean values of τ^λ and τ^ϕ underestimate the stress needed for proper mixing. The variability associated with the 12-hour forcing provides a mechanism for more intensive surface mixing.

Based on these experiments, the conclusion reached is that the high-frequency forcing is important for both heat flux and the vertical mixing scheme. The monthly mean forcing along with a parameterization of the high-frequency forcing would probably be successful in alleviating the problems associated with monthly mean data. However, even if the statistics of the wind field could be well represented over all geographic areas, some of the transient behavior of the real forcing would be lost. This could be important to a realistic simulation, for example the westerly wind bursts that appear in the western Pacific would not be captured.

Intercomparison with different models (A-physics and E-physics) but with the same forcing (12 hour) shows the overall performance of the E-12 model to be superior to the A-12. The thermal structure, SST, current speeds, and MLD are better reproduced by the E-12 model. However, the E-12 has its inadequacies, such as poor representation of the equatorial undercurrent not capturing the deep MLD and tight gradient of the thermocline in the western tropical Pacific and SST errors that are still appreciable. Nevertheless, it appears that by including SGS physics that better represent the physical mechanisms of mixing, a more realistic upper ocean simulation may be obtained.

The near-surface heat balance shows that the model reproduces the seasonal variations reasonably well. In the extratropics one-dimensional mixed-layer processes dominate, while in the tropics the balance is largely affected by the dynamics. The analysis also shows that the formation of large SST anomalies in the eastern equatorial Pacific are due to a combination of advection of heat and the surface heat flux. It is interesting to note that within the heat flux, thermal, and TKE balances, there are two terms that are large but whose difference is the same order of magnitude as the other terms. This implies that even errors in the smaller terms may have significant impact.

This study is considered preliminary, and a ten-year simulation that includes the 1982–83 El Niño is underway. Since the ocean GCM is not perfect and the boundary forcing is not perfect, it is difficult to ascertain the sources of errors. Our approach is to try to improve the model and external forcings wherever we can and then to verify from observations. This will be an iterative process where we hope the results will converge to the observations. It is within this framework that we will be investigating model improvements (diurnal variation, increased vertical and horizontal resolution); external forcing (data source, bulk formula exchange coefficients, 1000 mb versus surface data); and radiation improvements (inclusion of realistic cloud cover). Particular emphasis will be placed on obtaining the proper strength for the Equatorial Undercurrent.

Acknowledgments. The authors are especially grateful to G. Philander for his advice and review of the paper. We acknowledge K. Bryan and M. Cox for making the ocean model code available to us, J. Derber for the valuable discussions and review of the paper, and G. Mellor for technical advice. We also thank P. Tunison and J. Connor for help in preparing the figures, and W. Marshall for the expert typing of the manuscript.

REFERENCES

Adamec, D., R. L. Elsberry, R. W. Garwood, Jr. and R. L. Haney, 1981: An embedded mixed-layer-ocean circulation model. *Dyn. Atmos. Oceans*, **6**, 69–77.

Arakawa, A., and V. R. Lamb, 1977: Computational design of the basic dynamical processes of the UCLA general circulation model. *Methods in Computational Physics*, Vol. 17, Academic Press, 174–265.

Blanc, T. V., 1985: Variation of bulk-derived surface flux, stability and roughness results due to the rise of different transfer coefficient schemes. *J. Phys. Oceanogr.*, **15**, 650–669.

Blumberg, A. F., and G. L. Mellor, 1983: Diagnostic and prognostic numerical circulation studies of the South Atlantic Bight. *J. Geophys. Res.*, **88**(C8), 4575–4592.

Bryan, K., 1969: A numerical method for the study of the world ocean. *J. Comput. Phys.*, **4**, 347–376.

——, and L. J. Lewis, 1979: A water mass model of the world ocean. *J. Geophys. Res.*, **84**, 2503–2517.

Budyko, M. S., 1974: *Climate and Life.* Academic Press, 508 pp.

Bunker, A. F., 1976: Computations of surface energy flux and annual air–sea interaction cycles of the North Atlantic Ocean. *Mon. Wea. Rev.*, **104**, 1122–1140.

Cane, M. A., and E. Sarachik, 1976: Forced baroclinic ocean motions, I. *J. Mar. Res.*, **34**, 629–665.

——, S. E. Zebiak and S. C. Dolan, 1986: Experimental forecasts of El Niño. *Nature*, **321**, 827–832.

Cheney, R. E., and J. G. Marsh, 1983: Global mesoscale variability

from collinear tracks of SEASAT altimeter data. *J. Geophys. Res.*, **88**, 4343–4354.

Cox, M. D., 1984: A primitive equation, 3-dimensional model of the ocean. GFDL Ocean Group Tech. Rep. No. 1, 143 pp.

Crawford, W. R., and T. R. Osborn, 1981: Control of equatorial ocean currents by turbulent dissipation. *Science*, **212**, 539–540.

Deardorff, J. W., 1973: The use of subgrid transport equations in a three-dimensional model of atmospheric turbulence. *J. Fluid Eng., Sep.*, 429–438.

Derber, J. C., 1987: Practical data assimilation for the ocean. *Proc. Second WMO Workshop on the Diagnostics and Prediction of Monthly and Seasonal Atmospheric Variation over the Globe* and *WMO Symp. on Ocean-Atmosphere Interaction Relevant to Long-Range Forecasting*, Toulouse, France.

Esbensen, S. K., and V. Kushnir, 1981: The heat budget of the global ocean: An atlas based on estimates from surface marine observations. Climatic Research Institute, Oregon State University, Corvallis, Rep. 29, 27 pp.

——, and R. W. Reynolds, 1981: Estimating monthly averaged air–sea transfers of heat and momentum using the bulk aerodynamic method. *J. Phys. Oceanogr.*, **11**, 457–465.

Galperin, B., L. H. Kantha, S. Hassid and A. Rosati, 1988: A quasi-equilibrium turbulent energy model for geophysical flows. *J. Atmos. Sci.*, **45**, 55–62.

Garwood, R. W., 1979: Air–sea interaction and dynamics of the surface mixed layer. *Rev. Geophys. Space Phys.*, **17**, 1507–1524.

——, P. Muller and P. C. Gallacher, 1985: Wind direction and equilibrium mixed layer depth in the tropical Pacific Ocean. *J. Phys. Oceanogr.*, **15**, 1332–1338.

Gregg, M. C., H. Peters, J. C. Wesson, M. S. Oaky and T. J. Shay, 1985: Intensive measurements of turbulence and shear in the equatorial undercurrent. *Nature*, **318**, 140–144.

Halpern, D., 1987: Observations of annual and El Niño thermal and flow variations at 0°, 110°W and 0°, 95°W during 1980–1985. *J. Geophys. Res.*, **92**(C8), 8197–8212.

Haney, R. L., 1985: Midlatitude sea surface temperature anomalies: A numerical hindcast. *J. Phys. Oceaogr.*, **15**, 787–799.

——, and J. M. Wright, Jr., 1975: The relationship between the grid-size and the coefficient of nonlinear eddy viscosity in numerical ocean circulation models. *J. Comput. Phys.*, **19**, 257–266.

Hastenrath, S., and P. Lamb, 1978: *Climate Atlas of the Tropical Atlantic and Eastern Pacific Oceans.* University of Wisconsin Press, 122 pp.

Hellerman, S., and M. Rosenstein, 1983: Normal monthly windstress over the world ocean with error estimates. *J. Phys. Oceanogr.*, **13**, 1093–1104.

Hsuing, J., 1986: Mean surface energy fluxes over the global ocean. *J. Geophys. Res.*, **91**, 10 585–10 606.

Hughes, R. L., 1980: On the equatorial mixed layer. *Deep-Sea Res.*, **27A**, 1067–1078.

Jerlov, N. G., 1968: *Optical Oceanography.* Elsevier, 194 pp.

Levitus, S., 1982: *Climatological Atlas of the World Ocean.* NOAA Prof. Paper No. 13, U.S. Govt. Printing Office, 173 pp., 17 fiche.

List, R. J., 1958: *Smithsonian Meteorological Tables.* Smithsonian Institution, Washington, DC, 527 pp.

Lowe, P. R., 1977: An approximating polynomial for the computation of saturation vapor pressure. *J. Appl. Meteor.*, **16**, 100–103.

Martin, P. J., 1985: Simulation of the mixed layer at OWS November and Papa with several models. *J. Geophys. Res.*, **90**(C0), 903–916.

Meehl, G. A., and W. M. Washington, 1985: Sea surface temperatures computed by a simple ocean mixed layer coupled to an atmospheric GCM. *J. Phys. Oceanogr.*, **15**, 92–104.

Mellor, G. L., and T. Yamada, 1974: A hierarchy of turbulence closure models for planetary boundary layers. *J. Atmos. Sci.*, **31**, 1791–1806.

——, and ——, 1982: Development of a turbulence closure model for geophysical fluid problems. *Rev. Geophys. Space Phys.*, **20**, 851–875.

Mesinger, F., and A. Arakawa, 1976: Numerical methods used in atmospheric models. GARP Publ. Ser. No. 14, WMO/ICSU Joint Organizing Committee, 64 pp.

Miyakoda, K., and J. Suritis, 1977: Comparative integrations of global models with various parameterized processes of subgrid-scale vertical transports. *Beitr. Z. Phys. Atmos.*, **50**, 445–487.

——, and ——, 1983: Impact of subgrid-scale parameterizations on monthly forecasts. *Proc. ECMWF Workshop on Convection in Large-scale Numerical Models*, 231–277.

——, and A. Rosati, 1984: The variation of sea surface temperature in 1976 and 1977, 2. The simulation with mixed layer models. *J. Geophys. Res.*, **89**(C7), 6533–6542.

Moum, J. N., and D. R. Caldwell, 1985: Local influences on shear flow turbulence in the equatorial ocean. *Science*, **230**, 315–316.

——, ——, C. A. Paudson, T. K. Chereskin and L. A. Regier, 1986: Does ocean turbulence peak at the equator. *J. Phys. Oceanogr.*, **16**, 1991–1994.

Pacanowski, R., and S. G. H. Philander, 1981: Parameterization of vertical mixing in numerical models of tropical oceans. *J. Phys. Oceanogr.*, **11**, 1443–1451.

Paulson, E. A., and J. J. Simpson, 1977: Irradiance measurements in the upper ocean. *J. Phys. Oceanogr.*, **7**, 952–956.

Payne, R. E., 1972: Albedo of the sea surface. *J. Atmos. Sci.*, **29**, 959–970.

Philander, S. G. H., and R. C. Pacanowski, 1980: The generation of equatorial currents. *J. Geophys. Res.*, **85**(C2), 1123–1136.

——, and A. D. Seigel, 1985: Simulation of El Niño of 1982–83. *Coupled Ocean–Atmosphere Models*, ed. J. C. J. Nihoul, Elsevier Oceanography Series, Vol. 40, 517–541.

——, and R. C. Pacanowski, 1986: The mass and heat budget in a model of the tropical Atlantic Ocean. *J. Geophys. Res.*, **91**(C12), 14 212–14 220.

Reed, R. K., 1976: On estimations of net long-wave radiation from the ocean. *J. Geophys. Res.*, **81**, 5793–5794.

——, 1977: On estimating insolation over the ocean. *J. Phys. Oceanogr.*, **7**, 482–485.

——, 1983: Heat fluxes over the eastern tropical Pacific and aspects of the 1972 El Niño. *J. Geophys. Res.*, **88**, 9627–9638.

Reynolds, R. W., 1982: A monthly averaged climatology of sea surface temperatures. NOAA Tech. Rep. NWS 31, Washington, DC, 33 pp.

Sarmiento, J. L., 1986: On the North and Tropical Atlantic heat balance. *J. Geophys. Res.*, **91**(C10), 677–11 and (C11), p. 689.

Schopf, P. S., and M. A. Cane, 1983: On equatorial dynamics, mixed layer physics and sea surface temperature. *J. Phys. Oceanogr.*, **13**, 917–935.

Seckel, G. R., and F. H. Beaudry, 1973: The radiation from sun and sky over the North Pacific Ocean (abstract). *Trans. Amer. Geophys. Union*, **54**, p. 1114.

Semtner, A. J., 1974: An oceanic general circulation model with bottom topography. Numerical Simulation of Weather and Climate. Tech. Rep. No. 9, University of California, Los Angeles, 99 pp.

Simpson, J. J., and C. A. Paulson, 1979: Mid-ocean observations of atmosphere radiation. *Quart. J. Roy. Meteor. Soc.*, **105**, 487–502.

——, and T. D. Dickey, 1981: The relationship between downward irradiance and upper ocean structure. *J. Phys. Oceanogr.*, **11**, 309–323.

Smagorinsky, J., 1963: General circulation experiments with the primitive equations: I. The basic experiment. *Mon. Wea. Rev.*, **91**, 99–164.

Wajsowicz, R. C., 1986: Free planetary waves in finite-difference numerical models. *J. Phys. Oceanogr.*, **16**, 773–789.

Weare, B. C., P. T. Strub and M. D. Samuel, 1981: Annual mean surface heat flux in the tropical ocean. *J. Phys. Oceanogr.*, **11**, 705–717.

White, W. B., S. E. Pazan and M. Inoue, 1987: Hindcast/forecast of ENSO event based upon the redistribution of observed and model heat content in the western tropical Pacific 1964–1986. *J. Phys. Oceanogr.*, **17**, 264–280.